Temperature variations in caves induced by atmospheric pressure variations-Part 1: Transfer functions and their interpretation

Frédéric Perrier, François Bourges, Frédéric Girault, Jean-Louis Le Mouël, Dominique Genty, Bruno Lartiges, Rémi Losno, Stéphane Bonnet

Geosystems and Geoenvironment 2 (2023) 100145

Contents lists available at ScienceDirect

Geosystems and Geoenvironment

journal homepage: www.elsevier.com/locate/geogeo

Temperature variations in caves induced by atmospheric pressure variations—Part 1: Transfer functions and their interpretation

Frédéric Perrier[a,*], François Bourges[b], Frédéric Girault[a], Jean-Louis Le Mouël[a], Dominique Genty[c], Bruno Lartiges[d], Rémi Losno[a], Stéphane Bonnet[d]

[a] Université Paris Cité, Institut de Physique du Globe de Paris, CNRS, Paris F-75005, France
[b] Géologie Environnement Conseil, 30 rue de la République, Saint-Girons F-09200, France
[c] Environnements et Paléoenvironnements Océaniques et Continentaux, Université de Bordeaux, Pessac Cedex F-33615, France
[d] Université de Toulouse III Paul Sabatier, Géosciences Environnement-Toulouse, Toulouse F-31400, France

ARTICLE INFO

Article history:
Received 3 May 2022
Revised 22 September 2022
Accepted 21 October 2022

Handling Editor: A Festa

Keywords:
Atmospheric pressure
Natural ventilation
Preservation
Barometric pumping
Critical Zone
Phase changes

ABSTRACT

According to thermodynamics, atmospheric pressure variations (APV) cause temperature variations in air. However, such variations are difficult to observe, except in thermally stable environments such as underground cavities. We have studied the properties of these temperature variations in four natural caves in France, where continuous time-series have been collected since 1998: Esparros, Aven d'Orgnac, Pech Merle and Chauvet-Pont d'Arc Caves, the last two containing unique prehistoric wall paintings. The pressure to air temperature transfer function (TF), evaluated from 8×10^{-7} to 8×10^{-4} Hz, strongly depends on frequency; its modulus, at the barometric tide S2 (12 h), varies from 2 to 14×10^{-3} °C/hPa. While the TFs show pluriannual stability, seasonal variations are observed when sufficiently long data sets are available. Rock surface temperature is also affected by APV and we extract the air to rock surface temperature TF at Esparros, Chauvet and Pech Merle Caves. The observed TFs are accounted for by an improved analytical model including gas adiabatic compressibility, heat exchange with the rock, heat diffusion in the rock, phase changes of water at the rock surface and an advective term due to barometric pumping motion in the air volume. This model has three free parameters: the effective rock surface to air volume ratio, the time constant of heat exchanges and the effective adiabatic coefficient of cavity air. It is sufficient to account for the various situations observed in natural caves. Using this model, the observed TFs can be interpreted; they reflect the type of thermodynamics active at a given location, in particular the presence of barometric winds, but the actual values of parameters remain difficult to predict. Thus, temperature variations induced by APV emerge as a fundamental tool to characterize underground environments, relevant in some cases for cave heritage preservation, illustrating the coupled processes active in the Critical Zone.

1. Introduction

The Critical Zone (CZ), which extends from the upper parts of the aquifer to the top of the canopy, is the essential layer of continental Earth sustaining life (Lin, 2010; Xu and Liu, 2017). It is a complex physical system comprising rocks, soils, and biological material pervaded by geological and atmospheric fluids. This unique structure hosts numerous interaction modes and supports the emergence and the preservation of living species (Rasmussen et al., 2011; Zhang et al., 2017). Among the physical processes specific to the CZ, transport and thermal processes play a crucial role which is difficult to appreciate in the CZ internal part (Rasmussen et al., 2011; Lovill et al., 2018; Novitsky et al., 2018). Caves are open physical systems with varying boundary conditions (Andrieux, 1983; Mangin and D'Hulst, 1996; Mangin et al., 1999), which offer a unique and rare opportunity to access some of these CZ processes from inside (Zhang et al., 2017).

In underground systems, coupled processes involving heat and mass exchanges compete in a specific manner (Wigley and Brown, 1971; Perrier et al., 2002, 2004a; Luetscher et al., 2008), thus leading to complex dynamics including long- and short-term responses, stationary and transient states at the edge of stabil-

* Corresponding author: Pr. Frédéric Perrier, Institut de Physique du Globe de Paris, France
E-mail address: perrier@ipgp.fr (F. Perrier).

https://doi.org/10.1016/j.geogeo.2022.100145

ity, typical of out-of-equilibrium thermodynamics (Denis et al., 2005; Perrier et al., 2005b; Rasmussen et al., 2011; Perrier and Le Mouël, 2016). The physical behaviour of underground systems needs to be well understood in the context of geophysical observatories (Blum and Bérest, 1993; Trique et al., 1999; d'Oreye de Lantremange and Zuern, 2006; Niebauer et al., 2011) or deep underground physics observatories, for example in the search for new particles or dark matter (Bettini, 2014). Similarly, the stability and resilience of underground systems need detailed attention in practical applications such as underground geothermal energy research (Schill et al., 2016), as is the reliable assessment of the containment of underground nuclear waste repositories (Dupray et al., 2013; Bailly et al., 2014). Especially in the context of climate change, the long-term behaviour of caves is a fundamental issue for the preservation of natural sites hosting fragile ecosystems (De Freitas et al., 1982; De Freitas and Littlejohn, 1987), speleothems of scientific and touristic values (Bourges et al., 2006, 2014a; Genty, 2008) or precious prehistorical artwork and other early evidence of human social culture (Quindos et al., 1987; Bourges et al., 2014a, 2014b; Jaubert et al., 2016; Houillon et al., 2017; Hoffmann et al., 2018).

Recognized as early as 1783 by Jean-Dominique Cassini IV (1748-1845) while performing temperature measurements under the Paris Observatory with a precise thermometer specially built by Antoine Lavoisier (1743-1794), temperature is an essential parameter for the characterization of the temporal evolution of an underground system and of its deep or surface environment (Perrier et al., 2005a). Long-term temperature changes with pluriannual to decadal timescales have been observed underground in relation to climate changes (Badino, 2004; Beltrami et al., 2005; Dominguez-Villar et al., 2015) or solar cycles (Perrier et al., 2005a). However, their interpretation remains debated due to poorly known contributions such as groundwater flow (Bredehoeft and Papadopulos, 1965; Irvine et al., 2017) or urban island effects (Ferguson and Woodbury, 2004). Surface temperature variations such as the annual and faster variations, when transferred by heat diffusion, are rapidly attenuated with increasing depth (Perrier et al., 2005a).

Underground cavities are not isolated systems (Mangin and D'Hulst, 1996; Mangin et al., 1999; Badino and Chignola, 2019). Air circulation, resulting from temperature differences between internal and external atmospheres, appears near the entrance of caves; in vertical pits, they can take the form of turbulent plumes where they cause temperature variations with amplitudes larger than 1 °C and periods smaller than a few minutes (Perrier et al., 2002; Bourges et al., 2006). Quasi-stationary quasi-laminar air currents can be observed beyond 100 m distance from the entrance (De Freitas et al., 1982; Andrieux, 1983; Smithson, 1991; Kukuljan et al., 2021), especially in the case of subhorizontal tunnels (Perrier et al., 2005c, 2007), often inducing, in the entire cavity, seasonal temperature variations generally associated with changes in carbon dioxide (CO_2) and radon-222 concentrations (Fernandez et al., 1986; Perrier et al., 2004b; Perrier and Richon, 2010). Transient temperature changes associated with groundwater infiltration are observed near the entrance (Richon et al., 2009). Continuous temperature variations, with timescales from a few days to less than one hour, are commonly observed near the entrance of the cavities (Šebela and Turk, 2011). However, such variations result from atmospheric pressure variations (APV), which, because of the large air volume affected, cause large air motions near the entrance referred to as barometric wind (Conn, 1966; Badino and Chignola, 2019). Such barometric pumping or cave breathing effect (Wigley, 1967) can produce temperature variations as large as 1 °C/hPa near the entrance (Perrier and Le Mouël, 2016), with amplitudes decaying to less than 0.1 °C/hPa beyond 10 to 20 m in the underground system.

Deeper in the underground system, at a distance from the entrance or a depth greater than 100 m, extremely stable thermal conditions could be naively expected. Nevertheless, in addition to long-term variations, not straightforward to relate to surface long-term climate changes (Perrier et al., 2005a), temperature variations with amplitudes larger than 10^{-3} °C peak-to-peak, readily detected with currently available thermometers, are observed with timescales up to a few days (Perrier et al., 2001; Bourges et al., 2006; Šebela and Turk, 2011; Ravbar and Kosutnik, 2014; Drăguşin et al., 2018). This thermal signal is conspicuous during mid-latitude tempests (Perrier et al., 2001) or tropical typhoons (Perrier et al., 2004a). Such temperature variations result from APV, which cause thermodynamic adiabatic thermal changes in the air, damped by heat exchanges with the encasing rocks, leading to couplings of the order of a few 10^{-3} °C/hPa (Perrier et al., 2001). Phase changes of water, in saturated conditions, can significantly modify the amplitude of those pressure-induced temperature (PIT) variations (Perrier et al., 2001). These PIT variations generate, in reasonably thermally confined volumes, a characteristic noise pattern in time-series of underground air temperature and of rock surface temperature as well, which can be accounted for when heat diffusion in the encasing rock is considered (Perrier et al., 2010). At a given site, the amplitude of the PIT variations decreases in smaller cavities, increases with distance to the closest wall, and can exhibit a seasonal cycle (Perrier et al., 2010). The PIT response is characterized by a frequency-dependent transfer function, which can be modelled analytically (Perrier et al., 2001, 2010).

In this paper, we study the PIT response function in four natural caves situated in France: Esparros, Pech Merle, Aven d'Orgnac and Chauvet-Pont d'Arc Caves. Pech Merle and Chauvet Caves contain prehistoric paintings and need particular attention (Bourges et al., 2014a, 2014b, 2020). In these four caves, precise temperature data, in the atmosphere and at the rock surface, have been collected without interruption, at least since 1998. Taking advantage of the available time-series, complemented by temporary experiments, we establish the properties of the PIT variations and infer, at each site, reliable transfer functions (TFs) versus frequency. We then evaluate the significance of the TFs using a new expanded analytical physical model, whose relevance and limitations are discussed in details. Once the TFs are thus sufficiently well understood, the observed temperature variations can be used to correct the time-series for the PIT variations, a subject which is addressed in the companion paper (Perrier et al., this issue). In the present paper, we conclude by discussing the relevance of the TFs as a fruitful example of the type of coupled processes driving the dynamics of systems in the CZ.

2. Sites and methods

2.1. Description of the studied caves

The natural caves selected for this study are located in southern France (Fig. 1). Their geographical and geological settings have already been presented previously (Bourges et al., 2001, 2006, 2014a, 2014b, 2020). The characteristics of these caves relevant to the present analysis are briefly recalled below.

The Pech Merle painted Cave (44°30.45′ N, 1°48.67′ E) is located on the western edge of Massif Central in Oxfordian (Upper Jurassic) limestone and is characterized by an artificial entrance at an elevation of 284 m above sea level (asl.), equipped with a door, and a natural narrow opening at 302 m asl. (Bourges et al., 2014a). The cave system consists of two levels (Fig. 1a), connected by narrow conduits, which were expanded artificially after the discovery in 1922 to allow easier access. Only the lower level contains archaeological remains: parietal representations dated between 28,000

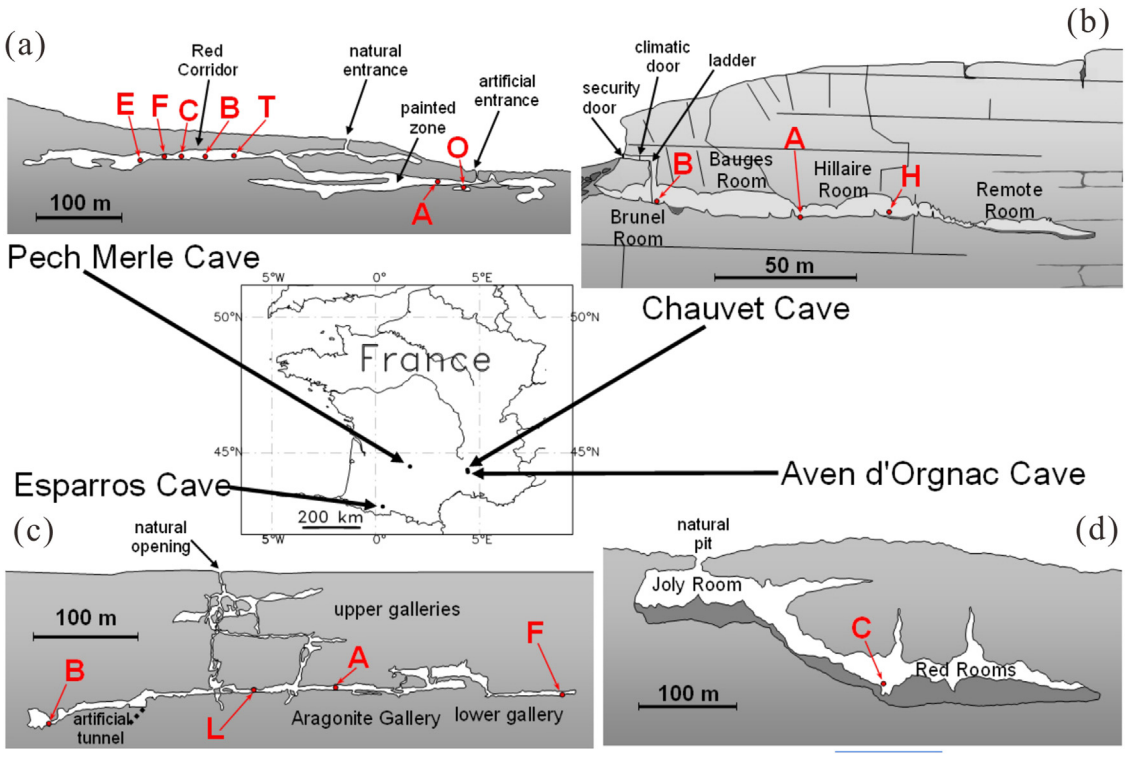

Fig. 1. Location of Pech Merle (a), Chauvet-Pont d'Arc (b), Esparros (c), and Aven d'Orgnac (d) Caves. A simplified cross-section of each cave shows the positions of sensors used in the present study. The cross-sections are derived from available topographic data and preliminary results from 3D surveys in progress. The location of the measurement points is indicated with capital letters in red.

and 22,000 BP (Lorblanchet, 2010), including characteristic negative hands, human artefacts and animal traces, as well as human footprints (Guineau et al., 2001; Pastoors et al., 2017). During prehistoric times, access to the cave was permitted from a collapsed pit and a debris cone, later obstructed. An artificial entrance closed by a door now leads the visitors to the sections containing paintings and archaeological remains. Some parts of archaeological value (e.g., "Ossuary", location O in Fig. 1a) are not accessible to the visitors. The upper level, which contains red clay filling ("Red Corridor"), while probably connected to the lower level during human prehistoric occupation, does not contain archaeological traces and is no longer included in the visitors' tour since 2007. It is connected to the surface by natural fissures enlarged by dissolution of the limestone, and contains numerous poorly known galleries. The total volume of the easily accessible section is estimated to exceed 40,000 m^3. The Pech Merle Cave is visited by more than 80,000 tourists per year, mainly from April to October.

The Chauvet-Pont d'Arc Cave (44.23°N, 4.26°E) is located in South-East France, on the left bank of the Ardèche River, a tributary of the Rhône River, in an Upper Barremian (Lower Cretaceous, Urgonian type) limestone cliff above an abandoned meander (Bourges et al., 2014a, 2014b; Clottes et al., 1995). The entrance (Fig. 1b) takes place through a narrow conduit above a slope collapse at an elevation of 200 m asl., which gives access from above to large rooms (Brunel, Bauges and Hillaire Rooms) with a floor at elevation from 186 to 188 m. A remote smaller room ("Remote Room"), with a floor at a lower elevation of about 178 m asl., is accessible through a small corridor ("Megaceros Corridor"). The cavity is covered by a 50 m thick layer of encasing rock at the edge of the plateau, reaching 70 m in the deepest parts of the cavity. The thickness of the topsoil layer ranges from a few decimetres up to 1 m at rare locations. The volume of the first set of chambers (Brunel, Bauges and Hillaire Rooms) is estimated to be about 60,000 ± 20,000 m^3, while the volume of the more isolated Remote Room (RR) amounts to about 2000 ± 500 m^3. All rooms are painted with sophisticated art pieces whose discovery, in 1994, caused a revolution in Paleolithic science (Clottes et al., 1995), revealing an extremely high level of refinement of paintings in the early period of Aurignacian (36,000 to 31,000 BP). In order to protect this precious heritage, the Chauvet Cave is not opened to visitors and access for archaeological research or maintenance is severely restricted (Bourges et al., 2014b, 2020).

The Gouffre d'Esparros Cave (43°1.8′ N, 0°19.8′ E), in the French Pyrenean foreland, is formed in Albian (Lower Cretaceous) low-magnesian calcite limestone that has undergone a slight metamorphism (Bourges et al., 2006). It has one main natural entrance, located at an elevation of 700 m asl., giving access to two superimposed levels of subhorizontal galleries (Fig. 1c) connected by vertical shafts: the upper and lower galleries are about 60 m and 130 m below surface level (bsl.), respectively. Visitors access the cave at 90 m bsl. by a 90-m long tunnel leading to the lower gallery. The "Aragonite Gallery" is the most remote part of the lower gallery, and is not part of the visitors' pathway. The total volume of the Esparros Cave system is estimated to exceed 30,000 m^3. The Esparros Cave sees more than 30,000 visitors per year.

The Aven d'Orgnac Cave (44°19.11′ N, 4°24.73′ E), characterized by its huge rooms in Aptian (Lower Cretaceous) limestone, is located 7 km South-East of the Chauvet Cave, on the right bank of the Ardèche River west of the Rhône River (Fig. 1d). It has a volume of at least 270,000 m^3, reaching depth as large as 120 m bsl., with a vertical access pit of 15 m height opening at the surface of the limestone plateau at an elevation of 300 m asl. (Bourges et al., 2001, 2006). The natural pit (called *aven* in old Celtic language) leads to the top of a huge room ("De Joly Room", named after the speleologist Robert de Joly), with spectacular speleothems up to 10 m high. A gently dipping slope gallery leads to a set of large rooms at a maximum depth of 120 m ("Red Rooms") with extensive red clay filling and large speleothems. The Aven d'Orgnac Cave is vis-

Table 1
Overview of the temperature measurements performed in the four caves investigated in this paper. The distance to the entrance is estimated from available topographic information. The modulus and phase of the transfer function, given for the semi-diurnal wave, correspond to the pressure to temperature (T_a/p) for air temperature sensors, and to air to rock temperature (T_r/T_a) for rock surface measurement, using the closest air temperature measurement. The mean atmospheric pressure is indicated for each site in the first column.

Location	Label	Distance to entrance (m)	Mean temperature (°C)	S2 Transfer Function		
				TF	Modulus	Phase (°)
Esparros Cave (956 ± 1 hPa)						
Aragonite Gallery A	$TEsA_a$	230	12.30 ± 0.01 (2006)	T_a/p	11.10 ± 0.36 10^{-3} °C hPa^{-1}	73.4 ± 1.1
	$TEsA_r$		12.31 ± 0.01 (2006)	T_r/T_a	0.094 ± 0.006	−26.1 ± 2.1
Above lake B	$TEsB_a$	120	13.14 ± 0.01 (2019)	T_a/p	4.46 ± 0.43 10^{-3} °C hPa^{-1}	87.8 ± 4.0
End Aragonite Gallery F	$TEsF_a$	500	11.59 ± 0.01 (2019)	T_a/p	1.65 ± 0.11 10^{-3} °C hPa^{-1}	69.9 ± 2.5
Aven d'Orgnac Cave (988 ± 1 hPa)			(1998-2000)			
Red Rooms point C	$TOrC_a$	200	12.29 ± 0.01	T_a/p	13.7 ± 1.9 10^{-3} °C hPa^{-1}	74.0 ± 7.2
Pech Merle Cave (986 ± 1 hPa)			(2017-2018)			
Beyond Red Rooms E	$TPmE_a$	242	12.10 ± 0.01	T_a/p	3.97 ± 0.14 10^{-3} °C hPa^{-1}	61.7 ± 3.0
End Red Rooms F	$TPmF_a$	212	12.24 ± 0.01	T_a/p	3.75 ± 0.18 10^{-3} °C hPa^{-1}	64.2 ± 4.5
Red Corridor C	$TPmC_a$	195	12.28 ± 0.01	T_a/p	3.46 ± 0.16 10^{-3} °C hPa^{-1}	63.9 ± 3.0
Red Corridor B	$TPmB_a$	160	12.33 ± 0.01	T_a/p	2.60 ± 0.14 10^{-3} °C hPa^{-1}	48.6 ± 4.5
Triplet T	$TPmT_{ref}$		12.34 ± 0.01	T_a/p	5.26 ± 0.18 10^{-3} °C hPa^{-1}	61.5 ± 2.8
	$TPmT_a$	140	12.36 ± 0.01	T_a/p	4.40 ± 0.16 10^{-3} °C hPa^{-1}	49.2 ± 2.7
	$TPmT_r$		12.35 ± 0.01	T_r/T_a	0.394 ± 0.010	−8.6 ± 1.2
Ossuary O	$TPmO_a$	26	13.20 ± 0.01	T_a/p	2.42 ± 0.16 10^{-3} °C hPa^{-1}	75.0 ± 3.1
Chauvet Cave (996 ± 1 hPa)			(2016-2019)			
Brunel Room B	$TChB_a$	25	13.89 ± 0.01	T_a/p	7.20 ± 0.21 10^{-3} °C hPa^{-1}	64.6 ± 1.6
	$TChB_r$		13.91 ± 0.01	T_r/T_a	0.186 ± 0.027	−1.9 ± 13
Hillaire Room H	$TChH_a$	100	13.05 ± 0.01	T_a/p	6.68 ± 0.24 10^{-3} °C hPa^{-1}	71.9 ± 1.1

ited by more than 140,000 (up to 160,000) tourists per year, which is nearly twice as much as the Pech Merle Cave and 5 times more than the Esparros Cave.

To summarize, Esparros, Pech Merle and Aven d'Orgnac Caves have two main levels with a natural permanently open pit at their top, whereas the Chauvet Cave has a basically horizontal structure with a single slightly higher entrance closed by a door. Pech Merle and Esparros Caves have a second artificial entrance at a lower level for the access of visitor groups and maintenance teams. Esparros, Pech Merle and Chauvet Caves have a moderate size smaller than 60,000 m^3, whereas the Aven d'Orgnac Cave is at least four times larger. The network of cavities connected to the Aven d'Orgnac Cave is considerably larger (about 8 times) than in the other caves.

2.2. Temperature and atmospheric pressure time-series

Continuous measurements of temperature at several underground locations in the atmosphere and at the rock surface are available, as well as relative humidity, atmospheric pressure and carbon dioxide concentration (CO_2), since 1996 at Aven d'Orgnac and Esparros Caves, since 1997 at the Chauvet Cave and since 1998 at the Pech Merle Cave. Additional data from temporary experiments performed between 2015 and 2018 complement the temperature time-series. In the present study, for the cases of Esparros, Aven d'Orgnac and Pech Merle Caves, only selected records collected outside of the visitor pathways and where the perturbations are minimal are used (Fig. 1 and Table 1). The sensors are labelled using the following convention. The first letter indicates the type of data ("T" for temperature, "p" for atmospheric pressure). The following two letters, with the first capitalized, indicate the site ("Es" for Esparros, "Pm" for Pech Merle, "Ch" for Chauvet and "Or" for Aven d'Orgnac Caves, respectively). The capital letter following the site name indicates the location within the site, as given in Fig. 1. Finally, an index indicates the type of measurement ("a" for measurement in air, "r" for measurement at the rock surface). For example, label $TEsA_a$ refers to the temperature measurement in the atmosphere of the Esparros Cave at location A. In this paper, we focus on a subset of the data available at each site (Table 1).

The same experimental set-up was used for long-term monitoring in all caves. Temperature was measured using platinum (Pt100) temperature sensors, regularly recalibrated, connected to an AOIP SA32 data logger and, after 2013 in Chauvet and Aven d'Orgnac Caves, to a Campbel Scientific™ CR3000 data logger (USA). Sampling interval was 15 minutes. The absolute precision of temperature is estimated to be about 0.05 °C with a relative precision of 0.01 °C and a sensitivity of 0.001 °C. At Esparros, Chauvet and Aven d'Orgnac Caves, the atmospheric pressure was measured, with a 15 min sampling interval, using a Druck™ PTX510 model (UK) and, after 2013, with a Vaisala™ PTB110 sensor (Finland). At the Pech Merle Cave, atmospheric pressure was measured with a BaroLogger™ model 3001 (Solinst, Canada) with a sampling interval of 5 minutes. In addition to the permanent set-up, complementary temperature data were acquired with autonomous SB recorders (with variants SB56, SB39 and SB39+) from Seabird™ (USA). Temperature measurement with these SB probes is performed using a high-precision thermistor with an absolute precision better than 10^{-3} °C, a relative precision better than 0.5×10^{-3} °C and a sensitivity of 10^{-4} °C. This probe can accumulate up to 300,000 data points with a sampling interval of 2 minutes. Possible long-term drifts of Pt100 are checked at regular yearly intervals, and corrected for when observed. No drift of SB probes was identified so far. In the present study, we are concerned with time-scales shorter than 20 days and drift artefacts of the sensors are therefore ruled out.

At the Esparros Cave (Es), temperature data from several locations were used. The most comprehensive records, starting in 1998, were located in the Aragonite Gallery (point A in Fig. 1c), with one temperature $TEsA_r$ at rock surface, taken 1 m above ground level, in a 5×6 m^2 section corridor, and one temperature $TEsA_a$ in the air taken 1 m horizontally away from $TEsA_r$. Atmospheric pressure was recorded at location L ("Lilas" Room), at the end of the section open to visitors. From September 2019, additional locations were

instrumented. In this paper, we give attention to the two most extreme locations in the Esparros Cave: point B above a permanent lake in the lowest part of the cave and point F at the end of the dead-end Aragonite Gallery. These locations were instrumented with SB39+, which simultaneously records atmospheric pressure.

At the Aven d'Orgnac Cave (Or), we used a single air temperature measurement $TORC_a$ situated 1 m above sediment base at location C in the red rooms section (Fig. 1d). In this section, the disturbance by visitors is minimal as well as the effect of turbulent air currents originating from the cave entrance in winter.

At the Chauvet Cave, the temperature has been monitored since 1997 at the rock surface and in the air in the first large room after the entrance, *i.e.* the Brunel Room ($TChB_a$ and $TChB_r$), and in the large central Hillaire Room ($TChH_a$ and $TChH_r$). The data from $TChH_r$ and the data recorded in the Remote Room (Fig. 1b), both affected by electronic noise, could not be used for high quality correlations (Table 1).

At the Pech Merle Cave, temperature has been recorded since 1998 in the painted section (point A in Fig. 1a) to monitor the impact of touristic frequentation, which includes the visitors themselves and the associated equipment such as lights and electrical distribution boxes. To get data at other locations away from the visitor pathway, additional autonomous SB probes (SB56, SB39 and SB39+) were used from 2015 to 2018 in non-visited parts (Fig. 1a and Table 1), i.e., in the upper level Red Corridor and in the Ossuary Room (O) at the lower level. At the same locations, simultaneous atmospheric pressure measurements were performed with some versions of the SB39 model and with the SB39+ model, which is a valuable asset for the present study, as will be shown below.

In addition, at the Pech Merle Cave, a particular SB39 assembly, referred to as the Triplet (Supplementary Data, Fig. S1), was installed at point T at the upper level (Red Corridor; Fig. 1a) in 2016 and 2017. The first SB39 temperature sensor was placed directly in contact with the rock surface ($TPmT_r$). The second SB39 temperature sensor was placed in the atmosphere ($TPmT_a$) at 3 cm from the rock surface, displaced laterally from $TPmT_r$ sensor by 3 cm. The third SB39 was attached to the previous SB39 pair, with the sensor pointing away from the surface, thus measuring the temperature $TPmT_{ref}$ in the atmosphere 30 cm away from $TPmT_a$ (Supplementary Data, Fig. S1). Unlike other temperature sensors mentioned previously at the rock surface (such as $TEsA_r$ or $TChH_r$), which were placed a few millimetres inside the rock, the $TPmT_r$ sensor was just touching the wall surface. The atmospheric pressure (labelled as "pPmT" or simply "pT" when the context in unambiguous) was simultaneously recorded by the SB39 providing $TPmT_{ref}$. The Triplet assembly was attached to the railing of a barrier to avoid undesired motions and to guaranty reproducible reinstallation after dismantling for data download, which was performed every six months.

2.3. Determination of the PIT transfer functions

The transfer functions (TFs) are calculated in the frequency domain using a robust algorithm (Supplementary Data, Appendix SA). Let us consider time-series a_i, b_i and c_i of N samples ($0 \le i \le N-1$) recorded over the same regular time base t_i with a sampling interval $\Delta t = t_{i+1} - t_i$. The set of N points is then divided into N_p non-overlapping sections. The TF $Z^c_{ab}(f_j)$ from b to a with reference c, at frequency $f_j = j/(N_p \Delta t)$, is then defined as (Sims et al., 1971):

$$Z^c_{ab}(f_j) = \frac{\sum_{k=0}^{N_p-1} \hat{a}_{j,k}\bar{\hat{c}}_{j,k}}{\sum_{k=0}^{N_p-1} \hat{b}_{j,k}\bar{\hat{c}}_{j,k}}, \quad (1)$$

where $\hat{x}_{j,k}$ is the complex discrete Fourier transform value at frequency f_j of the time-series x_i calculated from time section k with $0 \le k \le N_p-1$ (Crockett, 2019). The bar over the symbols in Eq. (1) refers to the complex conjugate. For the PIT TF from atmospheric pressure p to a given temperature T ($\hat{T}/\hat{p} = Z^p_{Tp}$), p is used as reference time-series. For the TF from air temperature T_a to rock temperature T_r ($\hat{T}_r/\hat{T}_a = Z^p_{T_rT_a}$), the atmospheric pressure p is used as reference time-series.

Using synthetic time-series with various noise properties, it can be shown (Supplementary Data, Appendix SA) that the TFs inferred from Eq. (1) are robust (Supplementary Data, Appendix SA, Fig. SA1). Precisely, robustness means here that the results are not affected by the presence of a reasonable level of noise, and that bad sections of data, where the calculated TFs are statistically incompatible with the average estimate, are automatically eliminated (Supplementary Data, Appendix SA). While a small value of N_p allows extending the frequency range to lower values, using larger values of N_p allows a better averaging and avoids bias of correlation in the presence of noise (Supplementary Data, Appendix SA, Fig. SA2). In this paper, we systematically check the stability of the results for various values of N_p, and we combine TF values estimated with small and large N_p values in order to establish reliable TFs over a large frequency range.

To evaluate the quality of the correlation, in addition to stability versus N_p, we use a simplified coherency as a function of frequency $C(f_j)$. This quantity, for the TF from b to a, is defined as (Perrier et al., 2010):

$$C(f_j) = \left| \frac{\sum_{k=0}^{N_p-1} \hat{a}_{j,k}\bar{\hat{b}}_{j,k}}{\sqrt{\sum_{k=0}^{N_p-1} \hat{a}_{j,k}\bar{\hat{a}}_{j,k}}\sqrt{\sum_{k=0}^{N_p-1} \hat{b}_{j,k}\bar{\hat{b}}_{j,k}}} \right|. \quad (2)$$

This definition allows in practice an efficient estimation of the quality of the TFs (Supplementary Data, Appendix SA). Coherency values depend on the site, the location within the site, the conditions of ventilation, the presence of visitors (regular tours or occasional maintenance) and on the particular variables selected. In general, as a rule of thumb, we require that the coherency must be larger than 0.5. In practice, we get coherency larger than 0.8 and stable values of TFs $\hat{T}/\hat{p}$ at all sites in reasonably thermally confined locations away from heavy visitor presence. The TF from air temperature T_a to rock temperature T_r ($\hat{T}_r/\hat{T}_a$), due to the small amplitude of variations at the rock surface ($<10^{-3}$ °C), is much more delicate to determine in a reliable manner, especially for frequencies larger than 10^{-4} Hz (2.8 hours). The use of pressure as reference is then necessary in the presence of noise (Supplementary Data, Appendix SA, Fig. SA3), and extra caution needs to be given in every case when evaluating the $\hat{T}_r/\hat{T}_a$ TFs.

Since only high-quality data were selected for the present work, uncertainties on the TFs are similar at all sites and measurement points. The uncertainty on the amplitude (Supplementary Data, Fig. S2a) varies from 10 to 20% for the lower frequencies (10^{-7} Hz), where the PIT response is low, to about 1% or smaller for the frequencies larger than 10^{-4} Hz, where the PIT response is the largest. Similarly, the uncertainty on the phase (Supplementary Data, Fig. S2b) decreases with frequency from a few degrees at frequencies around 10^{-7} Hz to about one degree or smaller for frequencies larger than 10^{-4} Hz.

Two additional problems need to be considered carefully. First, the time base needs to be the same for the considered time-series a and b (Supplementary Data, Appendix SA, Fig. SA4). While this is guaranteed when using the same data acquisition system, especially for a reasonably large sampling interval of 15 min, it is less obvious for independent SB probes at a sampling interval of 2 minutes. Consequently, initialization of probe clocks has to be done carefully. The second problem to be aware off is the difficult question of the homogeneity of the APV field in a large underground cavity. For frequencies lower than 10^{-4} Hz, the underground atmo-

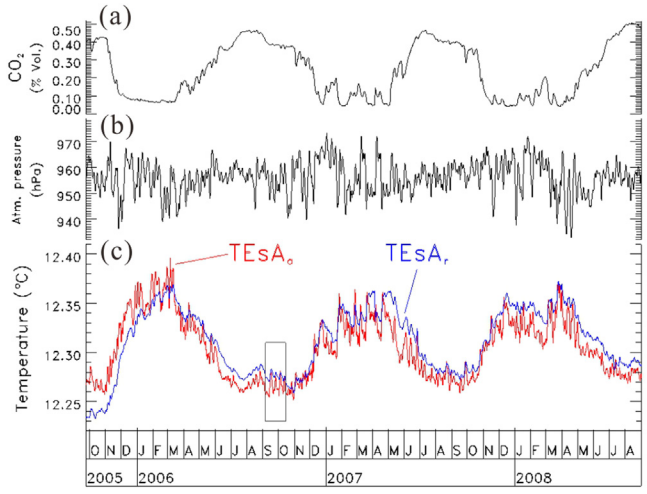

Fig. 2. Time-series at the Esparros Cave (point A in Fig. 1c) from 2005 to 2008 from the monitoring system operating with a sampling interval of 15 min: (a) CO_2 concentration recorded in the Lilas Corridor (point L in Fig. 1c), (b) atmospheric pressure recorded at point L, and air ($TEsA_a$) and (c) rock surface ($TEsA_r$) temperatures in the Aragonite Gallery. The time-series are averaged with a moving window of 48 h width. The rectangle shows the time section presented in Fig. 3.

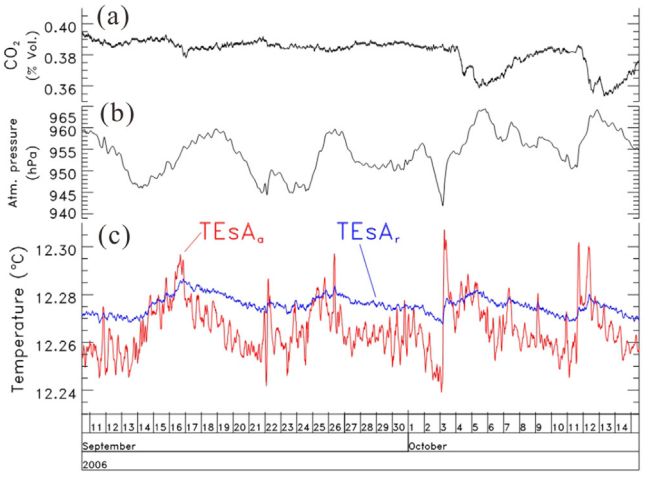

Fig. 3. Time-series at the Esparros Cave (point A in Fig. 1c) from September to October, 2006: (a) CO_2 concentration recorded in the Lilas Corridor (point L in Fig. 1c) and corrected for APV with a coefficient of 0.0015 hPa^{-1} % $conc.^{-1}$, (b) atmospheric pressure recorded at point L, and (c) air ($TEsA_a$) and rock surface ($TEsA_r$) temperatures in the Aragonite Gallery. The time-series are averaged with a moving window of 2 h width.

spheric pressure is homogeneous and synchronous with the surface atmospheric pressure. It is, however, less the case at frequencies higher than 10^{-4} Hz (Supplementary Data, Appendix SA, Fig. SA5), and significant differences can be evidenced when various atmospheric pressure sensors are compared. Part of this difference is likely due to the frequency response of each sensor. Furthermore, traveling pressure waves and resonances can appear in this high frequency range (Badino and Chignola, 2019). To establish proper TFs for frequencies larger than 10^{-4} Hz, it is therefore preferable, when possible, to use atmospheric pressure time-series recorded at the exact location of the temperature time-series, and, otherwise, to use the closest available pressure sensor.

3. Pressure-induced temperature transfer functions

3.1. PIT transfer functions in the Esparros Cave

High-quality continuous pluriannual temperature time-series were recorded at the Esparros Cave, especially in the Aragonite Gallery (Fig. 2). This cave is characterized by a seasonal ventilation cycle (Fig. 2c), with cold avalanches occurring in winter in the access pit. This entry of cold outside air in winter produces ventilation mixing in the whole cave and seasonal reduction of CO_2 concentration (Fig. 2a). The CO_2 peak value in summer does not exceed 0.5%, which is rather low but common in the context of limestone caves and especially of other caves in the Pyrenees mountains. Similar means and yearly amplitudes of CO_2 concentration were observed in the Lutetian limestone abandoned quarry of Vincennes near Paris (Perrier and Richon, 2010). The effect of APV on both air and rock temperatures is obvious in summer (Fig. 3), with larger response at high frequency, as expected from previous observations (Perrier et al., 2001; Bourges et al., 2006). The effect is about 10 times smaller on rock temperature $TEsA_r$ than on air temperature $TEsA_a$, but nevertheless easily observed, particularly during the brutal pressure drop of October 2-3, 2005 (Fig. 3).

The amplitude power spectra (Fig. 4) show a clear barometric tide S2 (12 h) both for air and rock temperatures, although with an amplitude 10 times smaller for $TEsA_r$. The semi-diurnal barometric tide S2, first pointed out by Lord Kelvin in 1882, is not a gravitational effect, but a thermal resonance (Lindzen and Chapman, 1969). The dominating presence of the semi-diurnal peak

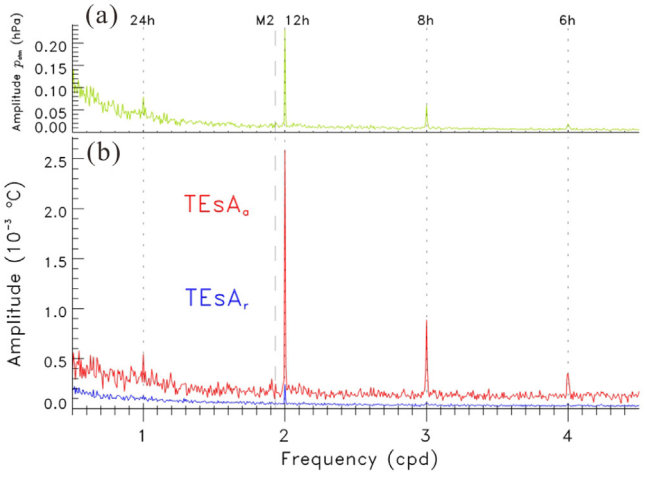

Fig. 4. Amplitude spectra as a function of frequency, expressed in cycle per day (cpd), at the Esparros Cave (point A in Fig. 1c) for the time period from September 2005 to September 2008: (a) atmospheric pressure recorded at point L, and (b) air ($TEsA_a$) and rock surface ($TEsA_r$) temperatures in the Aragonite Gallery. Spectra from data portions of 14,400 data points (150 days) are stacked to reduce continuum fluctuations.

S2 is the most conspicuous sign of PIT variations in temperature time-series (Mangin and D'Hulst, 1996; Perrier et al., 2001; Bourges et al., 2006), which always attracts attention in the first data from new sites (e.g., Sondag et al., 2003; Drăguşin et al., 2018; Mejía-Ortíz et al., 2020). From the ratio of the S2 peak for $TEsA_a$ (2.55×10^{-3} °C; Fig. 4b) to p (0.23 hPa; Fig. 4a), the PIT response can be estimated to be of the order of 11×10^{-3} °C/hPa. The lack of a S1 peak for $TEsA_r$ confirms that the site is thermally confined, with no obvious thermal signature of possible daily variations in the rate of natural ventilation. The S2 barometric tide can be directly observed on the pressure time-series (Fig. 5a), at Orgnac and Esparros Caves, and also in the temperature time-series simultaneously recorded at Aven d'Orgnac, Esparros and Chauvet Caves. (Fig. 5b). While the precise shape of the PIT response differs at both sites, with different high-frequency content, the S2 amplitude is similar at both sites and almost in phase. The S2 temperature variations at the three sites (Esparros, Chauvet and Orgnac), with Esparros Cave distant from Chauvet and Orgnac Caves by more

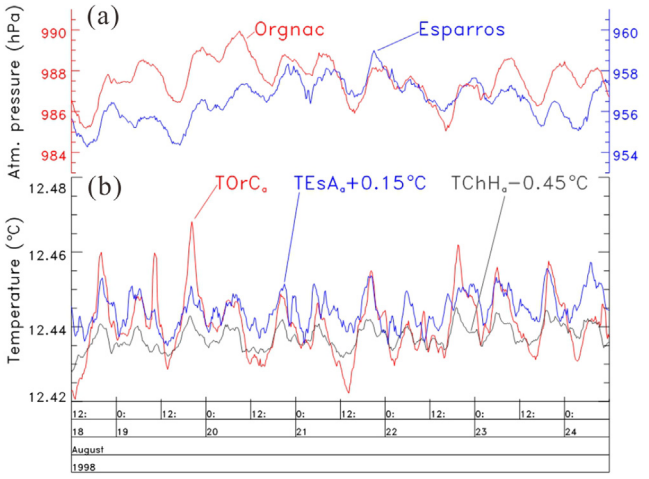

Fig. 5. Time-series at Esparros, Chauvet and Aven d'Orgnac Caves in August 1998: (a) atmospheric pressure, and (b) air temperatures. Atmospheric pressure at the Aven d'Orgnac Cave is measured in the "De Joly" Room (Fig. 1d). The time-series are averaged with a moving window of 1 h width.

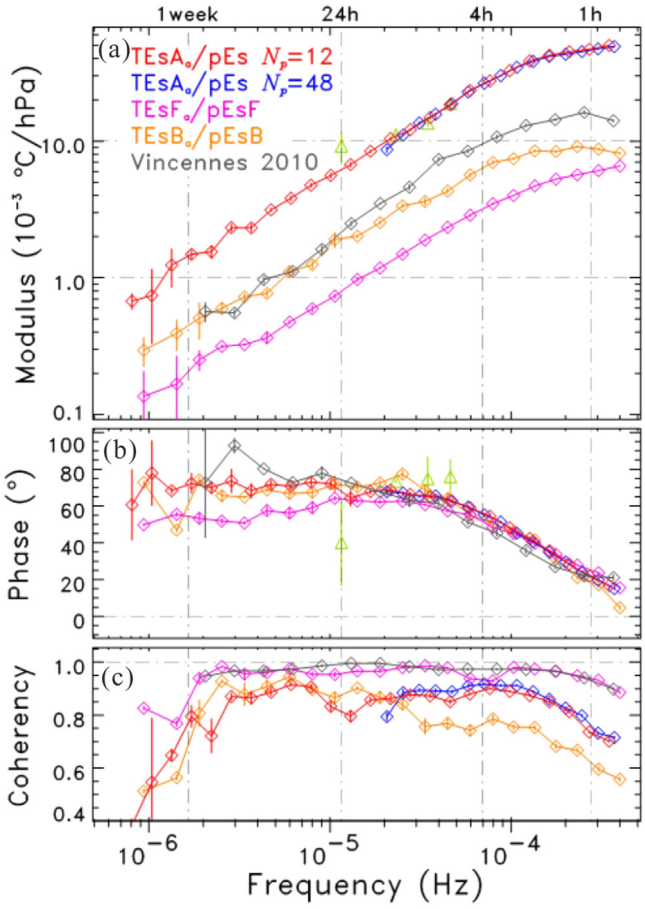

Fig. 6. Atmospheric pressure to air temperature TF versus frequency at the Esparros Cave: (a) modulus, (b) phase and (c) coherency. The time period from September, 2005 to September, 2008 is used for the TEsA$_a$/pEs with 12 data portions (in red) and 48 data portions (in blue). The green triangles for the TEsA$_a$/pEs TF correspond to the amplitude ratios for the S1 (24 h), S2 (12 h), S3 (8 h) and S4 (6 h) harmonic peaks. The TFs at the B and F points were obtained with data from September 2019 to June 2020, and TFs with 12 and 48 portions are combined. The TF in the Eve Room in the Vincennes Quarry near Paris (Perrier et al., 2010) is shown for comparison.

than 300 km, are remarkably similar (Fig. 5), due to the quasi-synchronicity of the S2 atmospheric pressure variation at this spatial scale. APV of longer timescales are much less correlated between Esparros and Orgnac sites (Fig. 5a); the associated temperature response, difficult to see in Fig. 5b, is largely dominated by the S2 signal.

The amplitude of the PIT TF versus frequency (Fig. 6), in a first approximation, is just the ratio of spectra, but the TF is actually a complex number and contains also phase information. The TF versus frequency, as produced by our algorithm, is of extremely high quality, smooth and stable over a large frequency range from 8×10^{-7} Hz to 4×10^{-4} Hz, with coherency larger than 0.8 from 2×10^{-6} Hz to 10^{-4} Hz. Increasing the value of N_p from 12 to 48 does not lead to any systematic difference, thus demonstrating the low level of noise in the TEsA$_a$ time-series. The TF at the Esparros Cave is remarkably stable over long periods of time (Supplementary Data, Fig. S3). After 2019, the TF could be determined precisely at the two other locations B and F (Fig. 1c) not affected by visitors. At location F, which is the deepest inside the mountain, coherency is larger than 0.95 over the whole considered frequency range (Fig. 6c). At location B, which is the lowest spot in the cavity and with a thinner rock coverage, estimated to be smaller than 20 m (Fig. 1c), the coherency decreases to values smaller than 0.8 for frequencies larger than 2×10^{-5} Hz. The presence of the lake and numerous infiltrations introduce probably other sources of temperature variations. While the phase response is similar at these two locations compared with the reference point A (Fig. 6b), the amplitude is significantly smaller, especially at point F.

The TFs at the Esparros Cave can be compared with the TF published previously at the Vincennes Quarry (Perrier et al., 2010). The variation of the phase with frequency is similar (Fig. 6b). The variation of the modulus with frequency is similar at both sites (Fig. 6a), but the amplitude is about three times larger at point A in the Esparros Cave, comparable at point B for frequencies smaller than 10^{-5} Hz, and a factor of two to four smaller at point F. While the coherency is comparable or larger at Vincennes (Fig. 6c), the longer time-series available in the Esparros Cave allow a precise determination over a larger frequency range. In the Vincennes Quarry, the amplitude of the TF was found to depend significantly on the observation point. However, the range of amplitudes between point A to point F in the Esparros Cave exceeds the previously observed range. Thus, the amplitude of the TF does not appear to be specific to a given cave, but characterises a type of dynamics at a given type of location in the underground system. This tentative conclusion is confirmed by our other observations below.

The result of the robust TF algorithm can be compared with the simple ratio of spectral amplitudes for the S1 to S4 peaks (in green in Fig. 6 for location A). The results from the S2 to S4 peaks (Fig. 6a, b) are in good agreement with the TF algorithm, better for the amplitude (Fig. 6a) than for the phase (Fig. 6b), whereas the ratio significantly differs from the TF algorithm for the S1 peak. This fact suggests that, albeit small in amplitude, other sources of variability exist for the S1 TEsA$_a$ temperature variations, such as, for example, thermal ventilation effects, air currents associated with the opening of the doors of the access tunnel, or some small thermal effects from visitors. In the following, to avoid contaminations of the PIT effect by harmonics of the daily variations when present, we concentrate interpretations on the S2 peak, and the results for the S2 response, calculated using this simple method of spectral amplitude ratio, are collected in Table 1.

The air to rock temperature TF can be determined using the high-quality time-series recorded at location A of the Esparros Cave (Fig. 7). In that case, because of the small amplitude of temperature signals at the rock surface (Fig. 3c), the coherency rapidly decreases for a frequency above 10^{-5} Hz (Fig. 7c). For larger frequencies, as demonstrated using synthetic signals (Supplementary

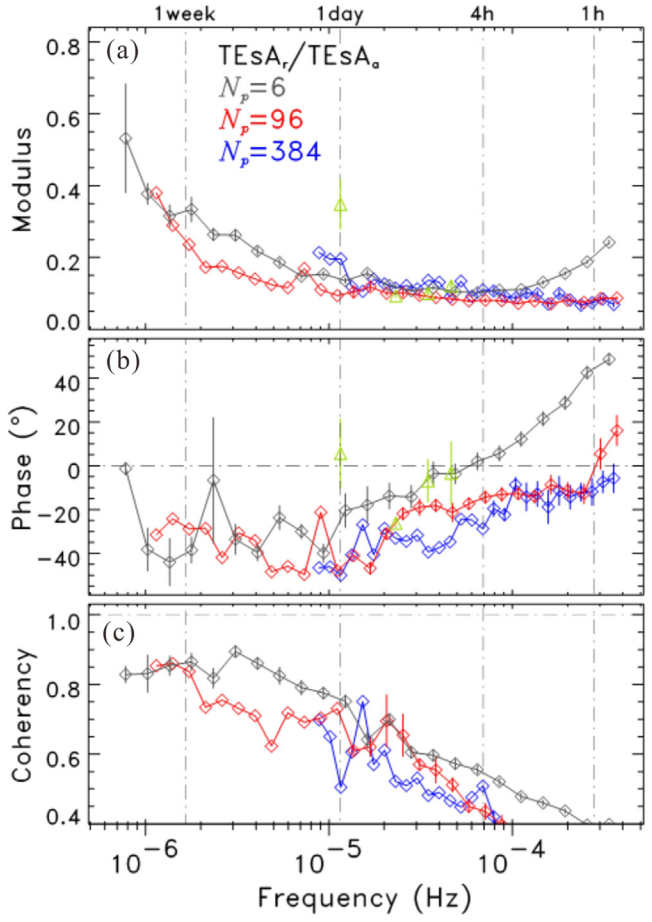

Fig. 7. Air temperature to rock surface temperature TF versus frequency at point A in the Esparros Cave for the time period from September 2005 to September 2008: (a) modulus, (b) phase and (c) coherency. The green triangles correspond to the amplitude ratios for the S1, S2, S3 and S4 harmonic peaks. Several configurations are compared, with atmospheric pressure as reference time-series in Eq. (1): 6 data portions (in grey), 96 data portions (in red) and 384 data portions (in blue).

Data, Appendix SA, Fig. SA3), it is necessary to use larger N_p values and to include p as correlation reference. With this caution, the TF remains stable when N_p is increased from 96 to 384, for both amplitude (Fig. 7a) and phase (Fig. 7b). The TF is remarkably stable over long periods of time (Supplementary Data, Fig. S3). A good agreement is again observed between the TF algorithm and the peak amplitude ratio for the S2 to S4 peaks (Fig. 7a, b), while the systematic disagreement for the S1 peak is confirmed in this case. For both $\hat{T}_a/\hat{p}$ and $\hat{T}_r/\hat{T}_a$ TFs, a sufficiently accurate estimate is achieved from the S2 peak ratios (Table 1) when a more precise determination of the TFs is not possible, for example when the duration of the available time-series is too small.

At the Esparros Cave, as sufficient data are available, the $\hat{T}_a/\hat{p}$ TF during summer (May to October) and winter (November to April) are well constrained separately. Consequently, small but clear and systematic differences are evidenced between the two seasons (Supplementary Data, Fig. S5). During summer, when the cave is more confined and CO_2 accumulates (Fig. 2), the amplitude of $\hat{T}_a/\hat{p}$ is lower by about 20% between 2×10^{-6} and 7×10^{-5} Hz and the coherency is smaller. A systematic shift of the phase towards slightly larger frequency is observed in summer (Supplementary Data, Fig. S5b). In contrast, for the $\hat{T}_r/\hat{T}_a$ TF, the amplitude and phase are similar between winter and summer (Supplementary Data, Fig. S6). The seasonal variation of the $\hat{T}_a/\hat{p}$ TF can also be evidenced convincingly using the simple S2 amplitude ratio in moving windows versus time (Supplementary Data, Fig. S7). The seasonal variation of the $\hat{T}_a/\hat{p}$ TF indicates that the underlying thermal process is modulated by ventilation, while it is not the case for the thermal process quantified by the $\hat{T}_r/\hat{T}_a$ TF.

3.2. PIT transfer functions in the other caves

Relying on the results at the Esparros Cave, the TFs at other sites are established in a systematic manner. In each case, for a given time-series, the TF is a combination of the results using a small N_p value (4 to 12) for low frequencies (from 8×10^{-7} Hz to 5×10^{-5} Hz) and the results using a sufficiently large N_p value (24 to 384) at high frequency (from 2×10^{-5} Hz to about 8×10^{-4} Hz, depending on the case). When several continuous time-series of similar quality are available at different time periods, all the results are averaged to calculate a final TF.

At the Aven d'Orgnac Cave, at point C (Fig. 1d), the results for $\hat{T}_a/\hat{p}$ TF versus frequency are similar to those at point A in the Esparros Cave, with similar amplitude and phase for the S2 wave (Table 1). A seasonal variation is clearly observed (Supplementary Data, Fig. S8), with larger amplitude up to about 40% during winter as in the Esparros Cave, but, constrasting with the Esparros Cave, only for frequencies larger than 10^{-5} Hz in the Aven d'Orgnac Cave, with a reduction during winter reaching 40% for frequencies below 10^{-5} Hz. TFs could not be achieved at other monitored locations in the Aven d'Orgnac Cave (De Joly Room), because they are affected, in summer, by the presence of large numbers of visitors and, in winter, by cold air avalanches entering the cave through the pit.

While, at Esparros and Aven d'Orgnac Caves, uninterrupted pluri-annual time-series are available from the permanent monitoring system, continuous time-series of six to eight months duration only are available with the autonomous SB probes at the Pech Merle Cave, but these shorter time-series are of high quality. The time-series recorded by the Triplet, in particular, illustrate the PIT variations with a remarkable precision for a sampling time of 2 minutes (Supplementary Data, Fig. S9). Several high-quality $\hat{T}_a/\hat{p}$ TFs were obtained in the Red Corridor at the upper level (Fig. 8), with coherencies larger than 0.7 over most of the frequency range, i.e., the largest set of high-quality PIT TFs determined so far in a single underground site. In the Ossuary Room (point O, Fig. 1a), located closer to the painted and visited section, the $\hat{T}_a/\hat{p}$ TF is of satisfactory quality, but with lower coherency and over a smaller frequency range (Fig. 8c). The mean temperature in the lower part of the Pech Merle Cave, which includes point O and the painted zone, is about 1 °C larger than the mean temperature in the upper section (Table 1), where temperature is rather uniform, especially in the Red Corridor. The TFs at the various points are different, significantly in amplitude (Fig. 8a), and moderately in phase (Fig. 8b). The modulus of the S2 response (Table 1) varies from $(2.60 \pm 0.14) \times 10^{-3}$ °C/hPa at point B and $(2.42 \pm 0.16) \times 10^{-3}$ °C/hPa at point O to $(5.26 \pm 0.18) \times 10^{-3}$ °C/hPa at $TPmT_{ref}$. In contrast, at the end part of the Red Corridor, from point E to C (Fig. 1a), the TF results are rather homogeneous. Clear differences are observed for the S2 phase from $(48.6 \pm 4.5)°$ at point B to $(75.0 \pm 3.1)°$ at point O (Table 1). At the location of the Triplet, a vertical profile of six regularly spaced SB56 recorders was also available during two months in 2017. While these data are insufficient to determine TFs versus frequency, the amplitude ratio at the S2 wave (Supplementary Data, Fig. S10) shows maximum values of about 6×10^{-3} °C/hPa in the central zone, with reductions to about 2×10^{-3} °C/hPa near the floor and the roof (Supplementary Data, Fig. S10). A similar vertical variation was previously observed at one location ("Room 15"), sufficiently well instrumented, of the Vincennes Quarry (Perrier et al., 2010).

Several $\hat{T}_r/\hat{T}_a$ TF are determined at the Pech Merle Cave using the data from the Triplet (Fig. 9). The highest coherency (larger

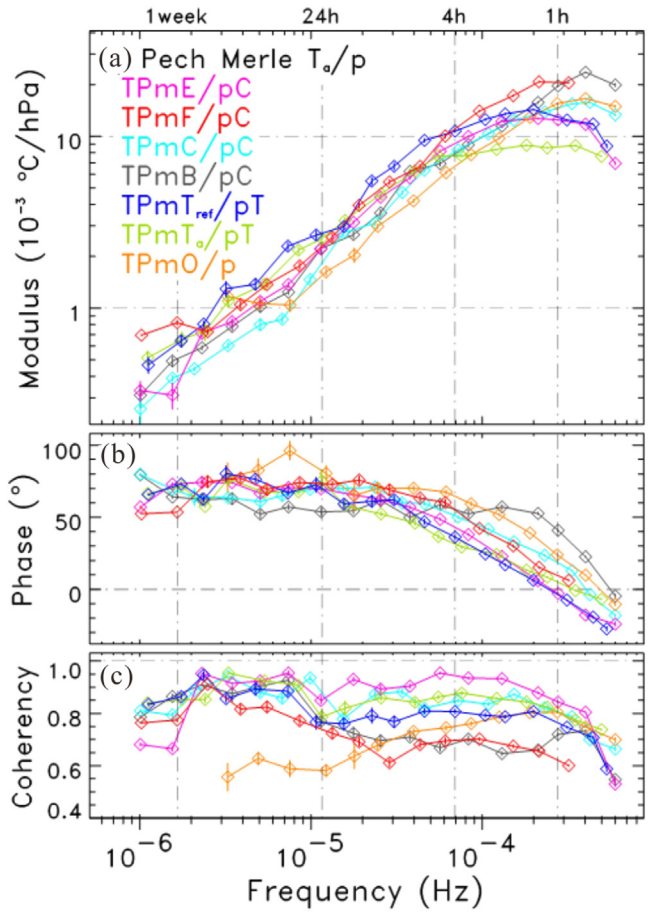

Fig. 8. Atmospheric pressure to air temperature TFs versus frequency at the Pech Merle Cave for the time period from October 2016 to December 2018: (a) modulus, (b) phase and (c) coherency. The closest available atmospheric pressure measurement is used (point C or T). In the case of the Ossuary Room (point O), atmospheric pressure was measured at point A in 2017 and at point D in 2018.

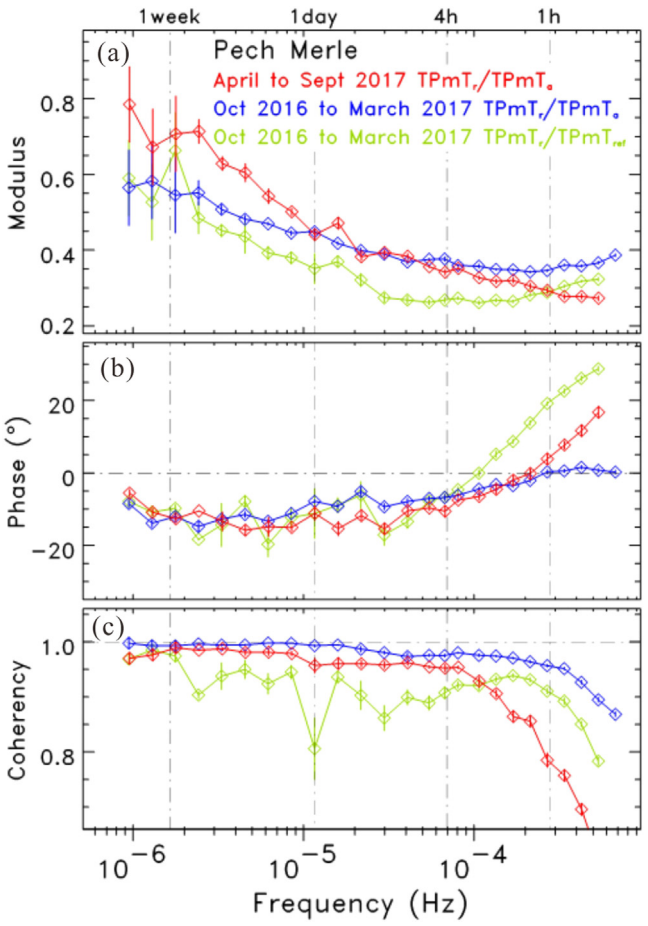

Fig. 9. Air temperature to rock surface temperature TFs versus frequency at the Pech Merle Cave, for several time periods, with the Triplet assembly at point T in the Red Corridor: (a) modulus, (b) phase and (c) coherency.

than 0.95 for frequency smaller than 3×10^{-4} Hz) is seen for the data-set from October 2016 to March 2017 for the $TPmT_a$ to $TPmT_r$ TF. Taking $TPmT_{ref}$ instead of $TPmT_a$, the TF shows a lower coherency and a suspicious phase pattern versus frequency for frequencies larger than 6×10^{-5} Hz, while modulus and phase are similar to $TPmT_r/TPmT_a$ for frequencies smaller than 7×10^{-5} Hz. Hereinafter, the most reliable $\hat{T}_r/\hat{T}_a$ TF, $TPmT_r/TPmT_a$ for the October 2016 to March 2017 data-set, is used. The modulus of the S2 response (Table 1) is 0.394 ± 0.010, which is significantly different from the value 0.094 ± 0.006 observed in the Aragonite Gallery (point A in Fig. 1c) at the Esparros Cave (Table 1).

In the Chauvet Cave, high-quality $\hat{T}_a/\hat{p}$ TFs are achieved (Fig. 10) for the two considered points B (Brunel Room) and H (Hillaire Room) (Fig. 1b). Amplitude and phase are similar over the whole frequency range for the Brunel ($TChB_a$) and Hillaire ($TChH_a$) Rooms, with a satisfactory coherency, larger than 0.75 for frequency smaller than 2×10^{-4} Hz. The highest coherency (>0.9) is observed for the Hillaire Room for frequency smaller than 8×10^{-5} Hz, probably more protected from other sources of variability. The $\hat{T}_a/\hat{p}$ TFs for $TChB_a$ and $TChH_a$ are remarkably stable over several years (Supplementary Data, Fig. S11), but a small difference appears between seasons, with an amplitude (22 ± 9)% larger in winter, constant over the whole frequency range (Supplementary Data, Fig. S12). The S2 amplitude and phase are similar for the two locations (Table 1), with values of the order of 7×10^{-3} °C/hPa and 70°, respectively.

A reasonably accurate $\hat{T}_r/\hat{T}_a$ TF at the Chauvet Cave can be determined for $TChB_r/TChB_a$ (Fig. 11), while the coherency decreases significantly for frequencies larger than 2×10^{-5} Hz (Fig. 11c). This TF is remarkably stable with time from 2015 to 2019 (Fig. 11), which suggests that, despite the reduced coherency, the TF remains reliable for frequencies larger than 2×10^{-5} Hz. It is also stable over seasonal timescales (Supplementary Data, Fig. S13). The modulus of the S2 $\hat{T}_r/\hat{T}_a$ response (Table 1), 0.186 ± 0.027, is significantly different from the values observed at Pech Merle or Esparros Caves.

3.3. Summary of the PIT transfer functions in the four caves

As we have used the same methodology, a comparison of the results at different locations in different caves is particularly meaningful. First, an overview of the S2 response reveals that amplitude and phase are interesting to consider simultaneously (Fig. 12 and Table 1), revealing that significant differences emerge between the various available measurements at a given site, especially in the case of the Esparros Cave, and between the various sites. Nevertheless, a typical amplitude value arises at each site: 4×10^{-3} °C/hPa at the Pech Merle Cave, 7×10^{-3} °C/hPa at the Chauvet Cave, and an upper value of about 10^{-2} °C/hPa at Esparros and Aven d'Orgnac Caves. However, as pointed out before, the amplitude is not representative of a given cave, but of a given type of location. For example, partly isolated locations of larger rooms (E to C in the Red Corridor of the Pech Merle Cave and Eve Room in the Vincennes Quarry) have amplitude of about 4×10^{-3} °C/hPa and a

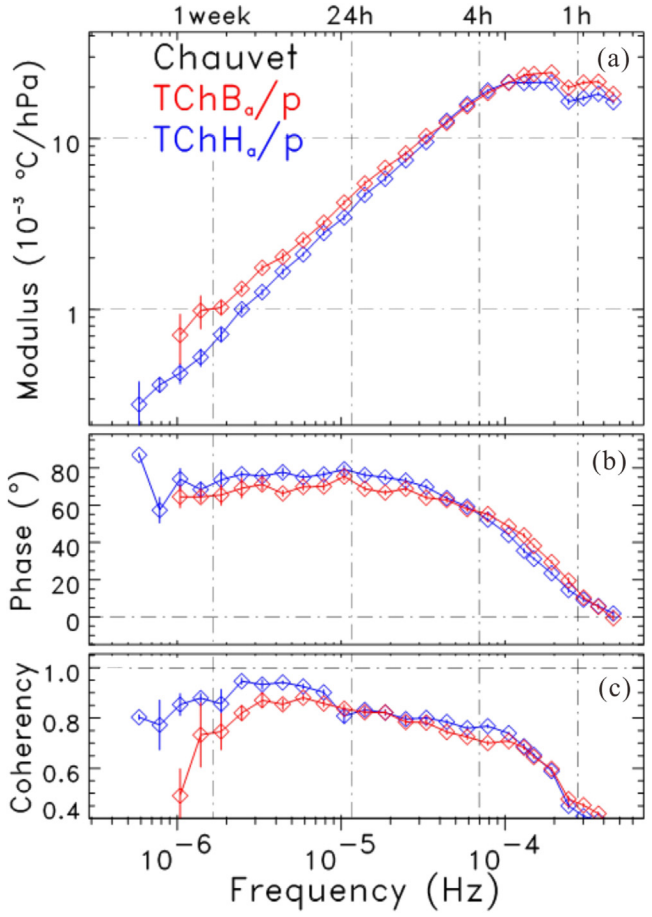

Fig. 10. Atmospheric pressure to air temperature TFs versus frequency at the Chauvet Cave in the Brunel Room (TChB$_a$/pCh in red) and in the Hillaire Room (TChH$_a$/pCh in blue): (a) modulus, (b) phase and (c) coherency. Results from time periods in 2015, from 2016 to 2017 and from 2018 to 2020 are averaged. Atmospheric pressure is measured in the Bauges Room (point A in Fig. 1b).

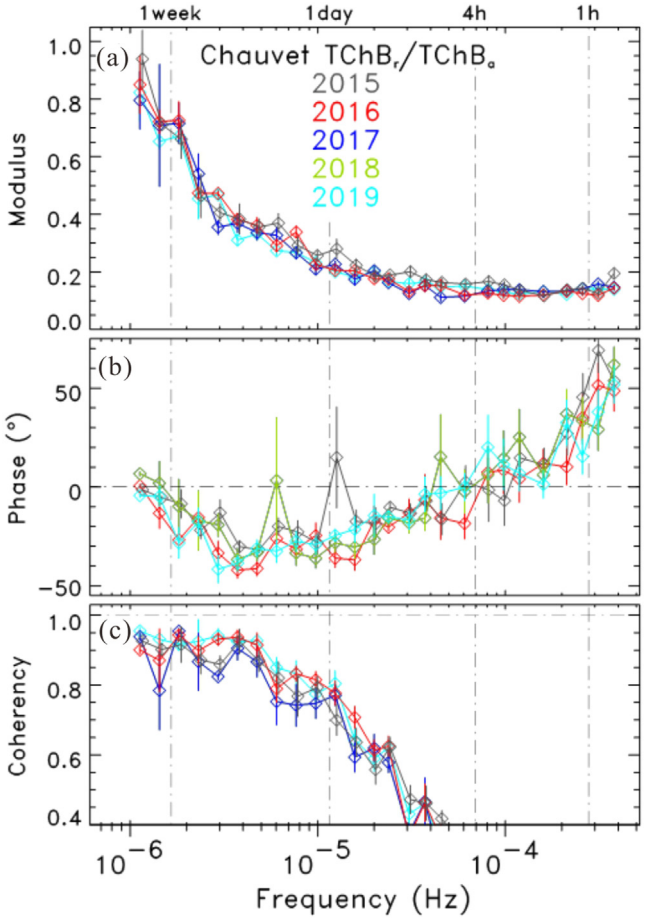

Fig. 11. Air temperature to rock surface temperature TF versus frequency at the Chauvet Cave in the Brunel Room (TChB$_r$/TChB$_a$), shown separately for several years from 2015 to 2019: (a) modulus, (b) phase and (c) coherency.

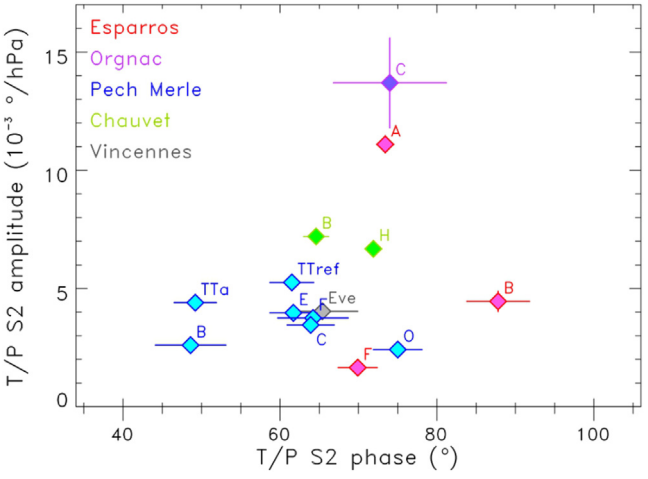

Fig. 12. Summary of the S2 PIT amplitude versus phase at the four studied caves. The result at the Eve Room of the Vincennes Quarry (Perrier et al., 2010) is shown for comparison.

phase near 65°, while extreme dead-end locations (O in the Pech Merle Cave and extreme point F in the Aragonite Gallery in the Esparros Cave) have amplitude of about 2×10^{-3} °C/hPa and a phase larger than 70°. The two locations in a large room, away from wall surfaces and in ventilated conditions (A point in the Esparros Cave and the considered point in the Aven d'Orgnac Cave) show a larger amplitude and a similar response in phase. It is difficult to draw, at this stage, firmer conclusions on the role of volume. Our model can only account for the effect of the cavity volume indirectly, through different thermal exchange times or enhanced barometric pumping velocities. Alternatively, the distance to the closest wall could be more important than air volume.

When selecting at each site a representative $\hat{T}_a/\hat{p}$ TF, having the highest-quality, *i.e.*, the largest coherency and the smoothest behaviour over the largest frequency range, significant differences are observed (Fig. 13). While the phase variation over frequency is similar for each site (Fig. 13b), with the Aven d'Orgnac Cave slightly separated from the other caves, large differences, with a factor from 4 to 5, can be noted for the modulus and its variation with frequency (Fig. 13a). The highest coherency (Fig. 13c) is attained at the Chauvet Cave for frequencies lower than 2×10^{-6} Hz and at Esparros and Pech Merle Caves for frequencies larger than 4×10^{-5} Hz.

For the $\hat{T}_r/\hat{T}_a$ TF, significant differences are revealed between the various sites (Fig. 14). The phase (Fig. 14b), frequency variation of the amplitude (Fig. 14a) and coherency (Fig. 14c) are similar for Esparros and Chauvet Caves, with slightly larger amplitude for the Chauvet Cave (Fig. 14a). The $\hat{T}_r/\hat{T}_a$ TF at the Pech Merle Cave with the Triplet is significantly different, with a much larger coherency (Fig. 14c) and a remarkably smoother frequency variation, especially for the phase (Fig. 14b). Given the small number of available $\hat{T}_r/\hat{T}_a$ TFs, and the difficulty in the determination of this TF, it is

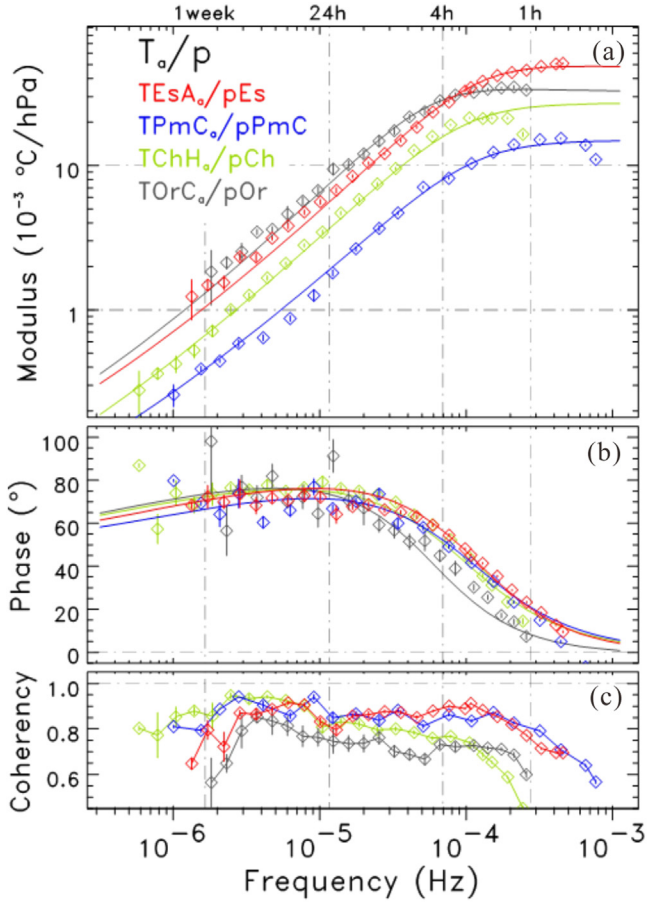

Fig. 13. Summary of representative atmospheric pressure to air temperature TFs versus frequency at the four sites studied in this paper: (a) modulus, (b) phase and (c) coherency. The curves represent the optimum theoretical analytical model given by Eq. (3) with the parameter values given in Table 2.

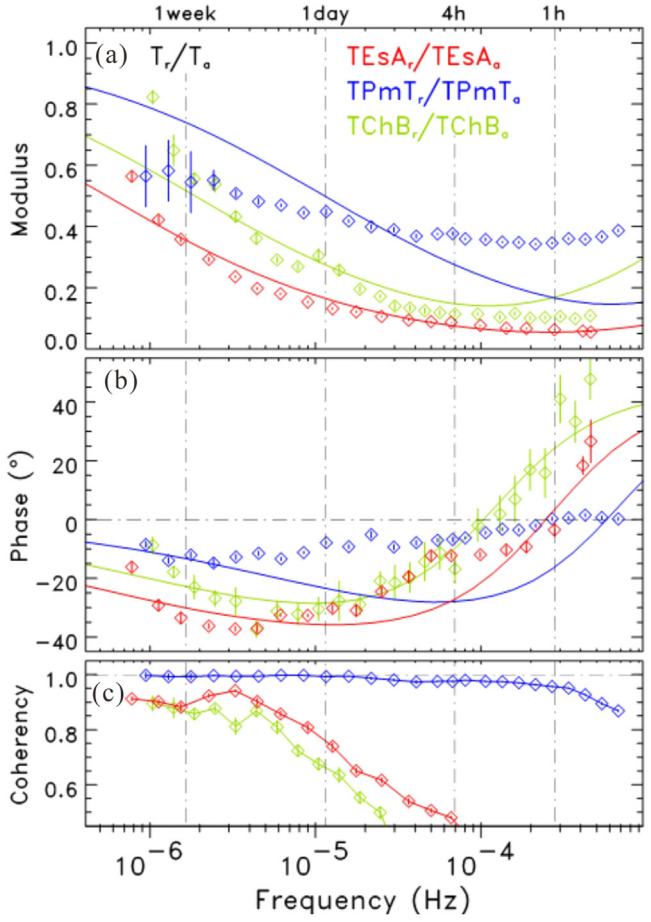

Fig. 14. Summary of representative air temperature to rock surface temperature TFs versus frequency at Esparros, Pech Merle and Chauvet Caves: (a) modulus, (b) phase and (c) coherency. The curves represent the optimum theoretical analytical model given by Eq. (3) with the parameter values given in Table 2.

premature to state whether the differences are due to meaningful differences between the points in the studied sites, or to the experimental configuration. Indeed, in Esparros and Chauvet Caves, the Pt100 sensor is inserted in a hole pierced in the rock wall in the Esparros Cave and in a sediment layer in the Chauvet Cave, while in the Pech Merle Cave, the sensitive part of the thermistor is in contact with the wall, with no hole or damage to the surface (Supplementary Data, Fig. S1). The thermal effect of the air boundary layer may modify the temperature response, and interpretation requires extra caution in this case.

4. Interpretation of the pressure-induced temperature transfer functions

4.1. Physical models of PIT transfer functions

The purpose of the physical model is to describe the processes contributing to the TFs and to provide explanations for the observed values and differences. To remove the PIT variations and extract residual time-series (see companion paper; Perrier et al., this issue), simple parameterizations of the TFs, separately for the modulus and the phase, are sufficient. However, an analytical expression of the TFs based on a physical model is valuable, particularly when the parameters possess a physical meaning and provide quantitative information on the systems.

Expanding upon previously established analytical models (Perrier et al., 2001, 2010), new analytical expressions for the TFs are proposed here (see details in Supplementary Data, Appendix SB), which include thermodynamic adiabatic heating, heat exchange with the rock, heat diffusion in the encasing rock, phase changes of water at the rock surface, with the addition of advection in the air volume due to barometric pumping (Supplementary Data, Appendix SB, Fig. SB1). When only isothermal barometric pumping is considered, and barometric pumping from the rock pore volume is neglected, the TFs have the following expressions (Supplementary Data, Appendix SB):

$$\begin{cases} \dfrac{\hat{T}_a}{\hat{p}} = \dfrac{\theta_{eff}}{1+\frac{1}{i\omega\tau}\left(1-\frac{\hat{T}_r}{\hat{T}_a}\right)} \\ \dfrac{\hat{T}_r}{\hat{T}_a} = \dfrac{1-b\frac{\theta}{\theta_{eff}}+\left(a-b\frac{\theta}{\theta_{eff}}\right)i\omega\tau}{1-b\frac{\theta}{\theta_{eff}}+\chi\tau\frac{S_r}{V_a}\sqrt{\frac{\kappa\omega}{2}}(1+i)} \end{cases}, \tag{3}$$

where $\omega = 2\pi f$, f is the frequency and $i = \sqrt{-1}$. The symbols with a hat refer to the Fourier component at frequency f. The quantities θ, κ, χ, a and b in Eqs. (3) are physical constants whose definitions are given in Supplementary Data, Appendix SB, Tables SB1-2). At 12 °C, we take $\theta = 83 \times 10^{-3}$ °C hPa^{-1} (adiabatic thermal expansion coefficient), $\kappa = 10^{-6}$ m^2/s (heat diffusivity in the rock) and $\chi = 1.6 \times 10^3$ (volumetric heat capacity ratio of rock to air). The constants a and b, without dimension, represent the contribution of evaporation and condensation of water vapour. At 12 °C, we have $a = 1.45$ and $b = 0.28$. When the contribution of phase changes of water is ignored, we take $a = b = 0$ in Eq. (3).

In addition, Eq. (3) for the TFs have three free parameters: θ_{eff}, τ and S_r/V_a. The parameter θ_{eff} gives the overall scale of the $\hat{T}_a/\hat{p}$ response. It is given by (Supplementary Data, Appendix SB):

$$\theta_{eff} = \theta + \frac{V_{eff}}{S_{eff}} \frac{\beta}{p_0}, \tag{4}$$

where p_0 is the mean atmospheric pressure, V_{eff} is the effective downstream cavity volume participating to barometric pumping, S_{eff} is the cavity section perpendicular to the pumping motion, and β is the static temperature gradient along the motion. The parameter θ_{eff} coincides with θ in the absence of advection. Conversely, a value of θ_{eff} that differs from θ indicates unambiguously the presence of barometric pumping motion in the air volume.

The parameter τ is the thermal relaxation time of the air volume. It is related to the effective conductance of the heat between the air volume and the encasing rock (Supplementary Data, Appendix SB). Finally, the parameter S_r/V_a is an effective thermal aspect ratio of the effective surface area S_r of rock in thermal interaction with a given air volume V_a. The various parameters affect differently the modulus and the phase of the TFs, and differently $\hat{T}_a/\hat{p}$ and $\hat{T}_r/\hat{T}_a$ TFs (Supplementary Data, Figs. SB2-4).

Two limiting behaviours as a function of frequency are of particular interest. At low frequency, the $\hat{T}_r/\hat{T}_a$ response from Eq. (3) converges towards an amplitude of 1 and a zero-degree phase shift. At high frequency, the amplitude should behave as $\sqrt{\omega}$ in the presence of phase changes of water, but converges to 0 when a=b=0. At high frequency, the $\hat{T}_a/\hat{p}$ response from Eq. (3) converges towards θ_{eff} and 0° phase shift. At low frequency, the $\hat{T}_a/\hat{p}$ modulus will tend to $\sqrt{\omega}$, and the phase will remain smaller than 90°, which is the maximum possible. When heat diffusion in the rock is ignored, the $\hat{T}_a/\hat{p}$ TF in Eqs. (3) converges at low frequency to $i\omega$, which is a pure time derivative with a linear variation in ω and a 90° phase shift (Perrier et al., 2001). This simplified situation of heat exchange with a temperature-stable reservoir, however, does not occur in underground caves. Indeed, the data unambiguously indicate a PIT response at the rock surface (Figs. 3 and 13).

4.2. Inversion of model parameters for the transfer functions

To fit the parameters to the $\hat{T}_a/\hat{p}$ TF data points versus frequency, the following process is used. Assuming isothermal barometric pumping, the phase of the TF depends only at second order on θ_{eff}, through the $\hat{T}_r/\hat{T}_a$ component in Eq. (3). Therefore, as a first hypothesis, an initial value θ_{eff}=θ_i is assumed. The calculated phase then depends little on the assumed value θ_i, whereas it affects the modulus by a global factor independent of frequency.

To find the optimal values of τ and S_r/V_a, independently of the overall factor on the amplitude controlled by θ_i, the following χ^2 is calculated as a function of τ and S_r/V_a:

$$\chi^2\left(\tau, \frac{S_r}{V_a}\right) = \sum_k \left(Fm\left(\tau, \frac{S_r}{V_a}, f_k\right) - m_k^{data}\right)^2 + \sum_k \left(p\left(\tau, \frac{S_r}{V_a}, f_k\right) - p_k^{data}\right)^2, \tag{5}$$

where m_k^{data} and p_k^{data} are the modulus and phase, respectively, measured at frequency f_k, $m(\tau, S_r/V_a, f_k)$ and $p(\tau, S_r/V_a, f_k)$ are the modulus and phase, respectively, calculated at frequency f_k from the given values of τ and S_r/V_a using Eq. (3). The factor F in Eq. (5) is defined as the average over k of the set of ratios $m_k^{data}/m(\tau, S_r/V_a, f_k)$.

The function $\chi^2(\tau, S_r/V_a)$ from Eq. (5), to a first approximation, is independent of θ_i. A minimization of χ^2 is then performed to find the best values of τ_{fit} and $(S_r/V_a)_{fit}$. The optimal value θ_{fit} is then equal to $F_{fit}\theta_i$, where F_{fit} is the average over k of the ratios $m_k^{data}/m(\tau_{fit}, (S_r/V_a)_{fit}, f_k)$. The minimization process can be iterated using a new assumption $\theta_I = \theta_{fit}$, but it was not found necessary in practice, as the change was smaller than the uncertainty. To estimate reasonable uncertainties on this determination, one or two points are removed at the edges of the frequency domain used for the fitting process. This estimate of the uncertainties was found appropriate by trial and error in each case.

The results of this adjustment of parameters on the experimental $\hat{T}_a/\hat{p}$ TFs are listed in Table 2 and the resulting TFs are shown as solid curves in Fig. 13. The uncertainties are different for each case, but vary from 1 to 10%, thus satisfactory and always smaller than the observed differences between the locations. When several TFs are available, the results of the fit are shown in Supplementary Data, Figs. S14-S16. The resulting adjustments appear satisfactory; not only reasonable values of the parameters, supporting their physical significance, are found, but the corresponding variations for the $\hat{T}_a/\hat{p}$ TFs as a function of frequency are remarkably consistent with the experimental data. In numerous cases in Esparros, Pech Merle and Chauvet Caves, however, an adequate representation of the data could only be attained when phase changes of water are not considered, *i.e.*, using $a = b = 0$ in Eq. (3). This may indicate that the processes active in the system are able to maintain a non-saturated atmosphere. When forcing phase changes of water, in such cases, the fits did not converge, largely because the frequency variation on the phase then became incompatible with the frequency variation of the modulus. Indeed, Eq. (3) predict rather different frequency variations with and without the phase changes of water (Supplementary Data, Appendix SB, Fig. SB3). In both Pech Merle and Chauvet Caves, it remains true for all available TFs. Non-saturated conditions are expected in the ventilated Pech Merle Cave, and are confirmed by relative humidity measurements at point A. It is more surprising in the confined Chauvet Cave, but it cannot be ruled out in the absence of high precision humidity measurements in the Hillaire Room. In the Brunel Room, humidity measurements indicated relative humidity values between 99 and 100%, thus excluding permanent saturation of the atmosphere. On the contrary, TFs at point A of Esparros Cave and point C of Aven d'Orgnac Cave favour the presence of phase changes of water.

On the whole, incorporating or not the phase changes of water, the various experimental situations can be described and, at all sites, the model described by Eq. (3) provides a correct description of the observed TFs (Fig. 13). In particular, the saturation of the modulus at high frequency ($f > 8 \times 10^{-5}$ Hz) is well accounted for. For frequencies lower than 10^{-5} Hz, the data show a smaller slope and a smaller phase for frequencies between 10^{-6} and 10^{-5} Hz compared with frequencies between 10^{-5} and 10^{-4} Hz. This flattening of the slope of the modulus at lower frequencies and the associated reduction of the phase advance are well reproduced by the theoretical expressions. This effect is due to the increasing contribution of heat diffusion in the rock when frequency decreases. The theoretical understanding of the $\hat{T}_a/\hat{p}$ TFs given by Eq. (3) thus appears sufficient and appropriate.

Reflecting the organization of the experimental data for the $\hat{T}_a/\hat{p}$ TFs (Table 1), the calculated values of the parameters are organized at a given site, and from site to site (Table 2). At the Pech Merle Cave, the $\hat{T}_a/\hat{p}$ TFs are characterized, in the Red Corridor, by S_r/V_a values between 0.07 and 0.13 m^{-1}. A similar S_r/V_a value (0.095 ± 0.032 m^{-1}) is inferred at the Esparros Cave, while a slightly larger value characterizes the Chauvet Cave (0.12 to 0.19 m^{-1}) and a smaller value (0.034 ± 0.008 m^{-1}) the Aven d'Orgnac Cave. The thermal relaxation time constant τ is similar at Pech Merle, Esparros and Chauvet Caves (about 20 min), but is about twice as large in the Aven d'Orgnac Cave. The longer thermal relaxation times do not show any clear relationship with the value of S_r/V_a or θ_{eff}, and could be due to the physical nature of the rock surface, for example the presence of wet films. The studied site with the strongest barometric advection, corresponding to the lowest values of θ_{eff} following Eq. (4), appears to be the Pech Merle

Table 2
Overview of the values of parameters for the models of transfer functions: pressure to temperature (T_a/p) for air temperature sensors, and air to rock temperature (T_r/T_a) for rock surface measurements.

Location	Transfer Function model parameters			
	TF	$\frac{S_r}{V_a}$ (m^{-1})	τ (minutes)	θ_{eff} (10^{-3} °C hPa^{-1})
Esparros Cave	a=1.45, b=0.28			
Aragonite Gallery A	$TEsA_a/pEs$	0.095 ± 0.032	22.1 ± 0.1	47.0 ± 0.5
	$TEsA_a/pEs$ Winter	0.063 ± 0.006	25.6 ± 0.1	44.2 ± 2.4
	$TEsA_a/pEs$ Summer	0.054± 0.023	19.8 ± 1.2	36.8 ± 3.8
	$TEsA_r/TEsA_a$	0.53 ± 0.02	5.2 ± 2.7	
	a=0, b=0			
Above lake B	$TEs_aB/pEsB$	0.067 ± 0.010	15.9 ± 0.3	6.64 ± 0.12
End Aragonite Gallery F	$TEsF_a/pEsF$	0.125 ± 0.005	22.2 ± 1.6	13.4 ± 0.5
Aven d'Orgnac Cave	a=1.45, b=0.28			
Red Rooms point C	$TOrC_a/pOr$	0.034 ± 0.008	45.1 ± 2.9	31.6 ± 0.7
Pech Merle Cave	a=0, b=0			
Beyond Red Rooms E	$TPmE_r/pPmC$	0.099 ± 0.018	43.7 ± 1.0	11.4 ± 0.3
End Red Rooms F	$TPmF_r/pPmC$	0.127 ± 0.020	24.8 ± 0.4	21.6 ± 0.5
Red Corridor C	$TPmC_r/pPmC$	0.131 ± 0.002	23.4 ± 0.1	14.9 ± 0.2
Red Corridor B	$TPmB_r/pPmC$	0.135 ± 0.040	20.2 ± 12.2	18.9 ± 7.8
Triplet T	$TPmT_{ref}/pPmT$	0.099 ± 0.008	55.7 ± 1.7	12.6 ± 0.3
	$TPmT_a/$ $pPmT$	0.073 ± 0.001	54.7 ± 1.2	10.1 ± 0.1
	$TPmT_r/TPmT_a$	0.20 ± 0.09	4 ± 1	
Ossuary O	$TPmO_a/pPmA$	0.53 ± 0.12	20.0 ± 1.4	18.2 ± 0.7
Chauvet Cave	a=0, b=0			
Brunel Room B	$TChB_a/pCh$	0.116 ± 0.003	25.3 ± 1.3	30.4 ± 1.4
	$TChB_r/TChB_a$	0.15 ± 0.02	12.5 ± 5.9	
Hillaire Room H	$TChH_a/pCh$	0.186 ± 0.003	27.2 ± 0.4	27.0 ± 0.5

Cave. This result is not surprising at the upper level of the Red Corridor, which is essentially a long corridor likely connected to vast unexplored volumes. However, it is unexpected in the case of the Ossuary Room, which is a small dead-end room, unless another connection with the surface is generated through the pore space, thus producing enhanced barometric motion in that location. Large barometric thermal damping is rather expected in the Chauvet Cave, located beneath a large volume of unsaturated rocks. This suggests, however, that the unsaturated zone is better connected downwards than to the surface. This fact indicates that the soil and the near-surface epikarstic aquifer pockets act, at least during some part of the seasonal cycle, as an efficient insulating membrane restricting exchanges with unsaturated volumes (Fernandez-Cortes et al., 2011). In contrast, large barometric motions are expected at both Aven d'Orgnac and Esparros Caves, where the instrumented locations are connected to large air volumes downstream.

In principle, the inferred values of θ_{eff} can be interpreted using Eq. (4) (Supplementary Data, Appendix SB). For example, for a static temperature gradient of β=−0.01 °C/m, an effective volume V_{eff} = 10,000 m^3, and an effective section S_{eff} = 4 m^2, we get $\theta_{eff} = \theta + \beta V_{eff}/(S_{eff} p_0) = 54 \times 10^{-3}$ °C/hPa (see above for the definitions of θ and p_0). In practice, this is useful only when the static temperature gradient is known at the measurement location. The value of S_{eff} can be estimated from the geometric configuration of walls at the considered location. An estimate of the effective pumping volume V_{eff} is then possible. This quantity V_{eff} is much more difficult to determine otherwise, as unexplored cavities downstream of the considered location can contribute. In the case of the Red Corridor at the Pech Merle Cave, we estimate S_{eff} = 9 m^2 and $\beta = -0.003$ °C/m from the various SB probes (Table 1) placed along the Red Corridor (Fig. 1a). The observed value of q_{eff} then constrains V_{eff} to be of the order of 180,000 m^3, which is unreasonably high despite the possibility of large unexplored cavities downstream. Furthermore, to guaranty $\beta < 0$, the direction of motion during pressure increases needs here to be towards the natural entrance of the cave. At this stage, the interpretation of θ_{eff} should therefore remain cautious.

To adjust the parameters of Eq. (3) using the $\hat{T}_r/\hat{T}_a$ TF data points versus frequency (Fig. 14), a similar minimization process is used. In this case, however, as the parameter values of θ_{eff} play only a minor role through the β parameter, it is sufficient to use an assumption, such as for example adopting the values derived from the fits of the $\hat{T}_a/\hat{p}$ TF. The minimization of χ^2, which is here defined as:

$$\chi^2\left(\tau, \frac{S_r}{V_a}\right) = \sum_k \left(m\left(\tau, \frac{S_r}{V_a}, f_k\right) - m_k^{data}\right)^2 + \sum_k \left(p\left(\tau, \frac{S_r}{V_a}, f_k\right) - p_k^{data}\right)^2, \quad (6)$$

involves only τ and S_r/V_a. Results are given in Table 2 and the corresponding TFs are shown versus frequency in Fig. 13. The curves given by the optimal values of the parameters provide a striking representation of the $\hat{T}_r/\hat{T}_a$ TFs for Esparros and Chauvet Caves. This result confirms the importance of the rock temperature variations to properly describe the PIT variations in air, as proposed through Eq. (3). The case of the Pech Merle Triplet $TPmT_r/TPmT_a$ is more problematic, as no proper fit of data could be achieved using Eq. (3). In that case, unlike the $\hat{T}_a/\hat{p}$ TF, removing the phase changes of water ($a = b = 0$) does not improve the agreement between the data and the model. Actually, for the Triplet T_r/T_a, phase changes of water are necessary, as otherwise the TF (see Supplementary Data, Appendix SB, Fig. SB2) becomes totally incompatible with the observations. This appears inconsistent with the conclusions reached from the $\hat{T}_a/\hat{p}$ TF at Pech Merle. However, the surface rock temperature which appears in the $\hat{T}_a/\hat{p}$ TF in Eqs. (3) refers to a representative mean temperature value of the whole rock surface contributing to the thermal equilibrium of the air volume, while the experimental $\hat{T}_r/\hat{T}_a$ TF represents a single particular location, which may or may not be representative of the whole cavity. The lack of proper representation of the $\hat{T}_r/\hat{T}_a$ TF definitely suggests, in the case of the Pech Merle Cave, some particular situation with the Triplet, an inappropriate measurement of rock temperature by mere contact, or some missing physics in the description of heat and matter exchanges at the rock surface.

5. Conclusions

5.1. Assessing the thermal response to atmospheric pressure variations in caves

In this study, we have used high-quality temperature time-series recorded in four caves of the South of France to investigate in details the temperature response to atmospheric pressure variations, both in the cave air and at the rock surface. We have obtained robust transfer functions from pressure to air temperature ($\hat{T}_a/\hat{p}$) and, for the first time, from air temperature to surface rock temperature ($\hat{T}_r/\hat{T}_a$) over three orders of magnitude of frequency, from 8×10^{-7} Hz to 8×10^{-4} Hz, thus extending and considerably improving previous results (Perrier et al., 2001, 2010). The quality of the $\hat{T}_a/\hat{p}$ TFs is particularly striking in Esparros and Chauvet Caves. Large variations, covering one order of magnitude in amplitude, from 2 to 14×10^{-3} °C/hPa at 12 hours, were observed between the various caves and between the various locations within a cave as well. At Esparros, Orgnac and Chauvet Caves where more than 20 years of data are available, pluriannual stability of the TFs and seasonal stability of the $\hat{T}_r/\hat{T}_a$ TF were observed. In addition, small but systematic seasonal variations of the $\hat{T}_a/\hat{p}$ TFs were evidenced, depending on the location and on frequency, with in general a reduction in summer compared with winter. This work confirms that, to study PIT variations properly, it is necessary to use temperature sensors with a sensitivity better than 10^{-3} °C and to acquire data with a sampling interval of 15 minutes or smaller, as was recommended in the nineties (Mangin and D'Hulst, 1996). Ideally, because of the seasonal effects, a minimum of three years of continuous and high-quality data is necessary. Long-term experiments over several decades would always be useful, especially to assess the effect of climate change (Badino, 2004; Perrier et al., 2005a), but this requires more considerable efforts.

5.2. Understanding the thermal response to atmospheric pressure variations in caves

The TFs versus frequency are in good agreement with an analytical physical model which includes air adiabatic temperature coefficient modified by heat exchanged with the rock surface, heat diffusion in the encasing rock, phase changes of water, and barometric pumping advection in the air volume. These thermodynamic processes are certainly present in the context of underground cavities, and they must be included in any modelling scheme. The interesting result, however, is that the model is able to describe the details of the observations, in particular the variation with frequency. It is sufficiently flexible to reproduce the variability of situations encountered in this study.

This model has three free parameters: the effective adiabatic compressibility θ_{eff}, the thermal relaxation time τ, and the effective rock surface to air volume ratio S_r/V_a. These three parameters can be inverted to account for the observed $\hat{T}_a/\hat{p}$ and $\hat{T}_r/\hat{T}_a$ TFs versus frequency, except the $\hat{T}_r/\hat{T}_a$ TF at the Pech Merle Cave which could not be accounted for by this model. This model assumes uniform PIT in the air volume and one-dimensional advection only. Components of velocity perpendicular to the wall surface may not be negligible, and turbulence may also complicate significantly barometric air currents, but it is not clear at this stage whether such complications can be incorporated in a meaningful and reasonably simple manner. The potential contribution of local wall breathing (Wigley, 1967) to thermal damping in the atmosphere, proposed long ago (Mangin and D'Hulst, 1996), is unlikely to be an efficient mechanism in nearly saturated rock conditions. The main limitations of our model, rather, should be examined in the basic assumptions on the heat exchange modes in an underground cavity. For example, heat exchange modes such as radiation (Villar et al., 1984), not explicitly taken into account, may play an important role. Water films flowing on the rock surface, or seeping locally from the encasing rock, may modify significantly the heat budget. In addition, the assumptions on the water phase changes may be too simplistic; it is possible that, in a given room, wet and dry walls coexist, with different reactions in terms of phase changes and rock surface temperature feedback. Evaporation on some wet wall may occur while condensation takes place on other dry wall surfaces, and conversely. Such effects will need to be looked into carefully with dedicated instrumentation in well-selected sites. Finally, the contribution of air circulation patterns may be over simplistic. Nevertheless, despite these possible sources of discrepancy between the analytical prediction and the data, the proposed physical model represents well the TFs at four different complex natural underground settings, which supports the concept that all the above considered effects are secondary. Our simplified analytical approach, thus, appears sufficient to address the apparent complexity and variability of the PIT frequency response in natural caves.

Less satisfactory, however, is the fact that the model cannot predict the actual values of the parameters, especially θ_{eff}. Furthermore, while current data consistently suggest that larger cavities or larger cave volumes lead to larger PIT response, there is no explanation at the moment for such an effect. Distance to the closest wall, rugosity of the cavity, presence of large speleothems or geometrical conditions favouring channelling of barometric air currents may also be important effects, which may cause the effect of volume to be coincidental. Dedicated experiments are needed to progress on this issue. Natural caves with their complex geometries may not be the best place to isolate such an effect, which was, for example, more convincingly observed in the Vincennes Quarry (Perrier et al., 2010).

5.3. Value of PIT response for cave preservation and cave modelling

Nevertheless, despite an incomplete physical understanding, the PIT TFs provide a phenomenological quantitative estimate of the thermal processes dominating at a given location of underground sites. In the Esparros Cave, the Aragonite Gallery shows larger PIT variations, while the most remote site, by contrast, shows reduced PIT response. Similarly, extended rooms with confinement conditions characterizing the Chauvet Cave, which guarantee the preservation of prehistoric artwork, are associated with an intermediate PIT response. Thus, the PIT TFs provide an assessment of the local conditions, and should be considered as an essential prerequisite in numerous applications, especially when there is a major preservation issue. The seasonal variation of PIT TFs appears as an additional proxy to qualitatively confirm the presence of seasonal quasi-static or of pressure dependent air currents. In all cases, the PIT response provides a quantitative estimate for the thermal relaxation time constant at a given location in the atmosphere, characterizing effectively the heat exchange with the associated rock surface. The numerical values can then be used to estimate the temperature change associated with a given heat source, natural or artificial (Crouzeix et al., 2003, 2006). Consequently, from the PIT variations, the heating effect associated with a group of visitors can be directly estimated and compared with observations.

PIT variations are useful to study and monitor in all underground sites because they are always present and stand out in the time-series as soon as the thermal environment is sufficiently stable. In terms of physics, as discussed above, they offer a subtle example of coupled processes which is a dominant aspect of the physics approach relevant in natural sites. This analysis in terms of elementary processes is compatible with other possible approaches, such as global modelling inspired by non-linear dynamics (Sáez et al., 2021; Turcotte, 1992) or decomposition tech-

niques (Ghil et al., 2002; Crockett et al., 2010), which work out interpretations from the time-series. Rather, one may expect that these different approaches contribute to revealing complementary aspects, and both will ultimately converge to consistent quantitative predictions.

Finally, PIT variations are useful to consider in a broader perspective, because APV affect numerous parameters in an underground cavity, not only temperature. Significant ground deformation signals are associated with APV (Dal Moro and Zadro, 1998) as well as variations of aquifer piezometric levels (Quilty and Roeloffs, 1991). Groundwater drippings, which are an essential component of an underground cavity in the unsaturated zone, are also affected by APV (Genty and Deflandre, 1998). To fully understand the dynamics of speleothem growth (Genty et al., 2001; Rau et al., 2015), an approach combining APV and temperature measurements with hydrological and geochemical parameters is desirable. APV, therefore, emerge as a natural permanent source of forcing applied to a natural site, even at great depth, which can be used to probe this system. Thus, APV are similar to the natural electromagnetic waves which permanently illuminate a surface system and are used in magneto-telluric sounding to probe the electrical conductivity structure of the crust (e.g., Berdichevsky and Dmitriev, 2008). PIT response and its modulation provide a thermobarographic sounding of the considered system and illustrate the variety of processes taking place in underground caves. The PIT response therefore is a systematic tool to use in a global approach attempting a comprehensive understanding of the CZ, which we slowly learn to appreciate as the complex, particularly rich but fragile outer interface of our planet.

Author Statement

First author designed the study, did the analysis and wrote the paper. François Bourges coordinated since 1995 all experiments in the four caves and prepared the time-series. Dominique Genty and Bruno Lartiges coordinated the scientific programs in Chauvet and Esparros caves, respectively. Jean-Louis Le Mouël developed the theoretical models with the first author since 1999. Frédéric Girault and Rémi Losno participated in the experiments and in the installation and recovery of temporary sensors. Stéphane Bonnet participated in the geological analysis and carried out the 3D topographic surveys. All co-authors contributed in the interpretations and their refinements, edited and corrected the manuscript's text and figures.

Declaration of Competing Interest

The authors declare that they have no known competing financial interests or personal relationships that could have appeared to influence the work reported in this paper

Acknowledgements

This work contributes to the IdEx Université de Paris *ANR-18-IDEX-0001*. The authors express their gratitude to Joël Ughetto and Stéphane Tocino at the Aven d'Orgnac Cave, to Dominique Baffier, Marie Bardisa, Charles Chauveau, Paulo Rodrigues and the scientific team coordinated by Carole Fritz at the Chauvet Cave, to Bertrand Defois and the late Jean-Luc Zimmermann at the Pech Merle Cave, and to Francis Ferran, Danielle Forgue and Federica Hanrard at the Esparros Cave. The speleological team (Jean-Pierre Bermond-Gonnet, Josiane Dassain and Adrien Lorentz) is thanked for their highly technical assistance to access the remote parts of the Esparros Cave. François Bourges thanks Eric Mauduit and Pascal Foucher at the DRAC Occitanie Services and the members of Laboratoire de Recherche sur les Monuments Historiques from the French Ministry of Culture for their support over the years. Work in the Esparros Cave was supported in part by the French National program EC2CO HYBIGE PAGE "Paradoxe Aérologique dans le Gouffre d'Esparros". Patrick Richon from CEA/DASE is thanked for the Seabird^{TM} SB39+ sensors used in this study, and Edouard Régnier from CEA/LSCE is thanked for his assistance. The help of students, Brian Asghar, Camille Bourges, Camille Fabre, Estelle Fourment, Camille Gaudinat, Julie Enjalbert and William Hedin, is acknowledged during field operations. Pierre Morat is thanked for his pioneering work in underground cavities and the inspiration given to the first author. The original version of this manuscript was improved thanks to the careful and informed work of the Associate Editor Andrea Festa and two anonymous reviewers. This work is GIS-GEMS contribution number 1.

Supplementary materials

Supplementary material associated with this article can be found, in the online version, at doi:10.1016/j.geogeo.2022.100145.

References

Andrieux, C., 1983. The air movements in the "Grotte de Niaux" - Consequences. Karstol. 1, 19–24.
Badino, G., 2004. Cave temperatures and global climatic change. Int. J. Speleol. 33, 103–114.
Badino, G., Chignola, R., 2019. Fluctuations of atmospheric pressure and the sound of underground karst systems: The Antro del Corchia (Apuane Alps, Italy). Front. Earth Sci. 7, 147.
Bailly, D., Matray, J.-M., Ababou, R., 2014. Temporal behavior of a ventilated claystone at the Tournemire URL: Cross-spectral analyses focused on daily harmonics. Eng. Geol. 183, 137–158.
Beltrami, H., Ferguson, G., Harris, R.N., 2005. Long-term tracking of climate change by underground temperatures. Geophys. Res. Lett. 32, L19707.
Berdichevsky, M., Dmitriev, V.I., 2008. Models and Methods of Magnetotellurics. Springer-Verlag, Berlin Heidelberg.
Bettini, A., 2014. New underground laboratories: Europe, Asia and the. Americas. Phys. Dark Universe 4, 36–40.
Blum, P.-A., Bérest, P., 1993. Measurement of the deformations of a cavern induced by Earth tides. C. R. Acad. Sci. Paris 316, 1341–1347.
Bourges, F., Genthon, P., Mangin, A., D'Hulst, D., 2006. Microclimate of l'Aven d'Orgnac and other French limestone caves (Chauvet, Esparros, Marsoulas). Int. J. Climatol. 26, 1651–1670.
Bourges, F., Genthon, P., Genty, D., Lorblanchet, M., Mauduit, E., D'Hulst, D., 2014a. Conservation of prehistoric caves and stability of their inner climate: Lessons from Chauvet and other French caves. Sci. Total Environ. 493, 79–91.
Bourges, F., Genty, D., Perrier, F., Lartiges, B., Régnier, E., François, A., Leplat, J., Touron, S., Bousta, F., Massault, M., Delmotte, M., Dumoulin, J.-P., Girault, F., Ramonet, M., Chauveau, C., Rodrigues, P., 2020. Hydrogeological control on carbon dioxide input into the Chauvet-Pont d'Arc cave. Sci. Total Environ. 716, 136844.
Bourges, F., Mangin, A., D'Hulst, D., 2001. Carbon dioxide in karst cavity atmosphere dynamics: the example of the Aven d'Orgnac (Ardèche). C. R. Acad. Sci. Paris 333, 685–692.
Bourges, F., Mangin, A., Genthon, P., Genty, D., D'Hulst, D., Mauduit, E., 2014b. Conservation and handling of decorated prehistoric caves: lessons from environmental monitoring at Chauvet-Pont d'Arc cave. Paleo Special Issue 339–345.
Bredehoeft, J.D., Papadopulos, I.S., 1965. Rates of vertical groundwater movement estimated from the Earth's thermal profile. Water Resour. Res. 1, 325–328.
Clottes, J., Chauvet, J.-M., Brunel-Deschamps, E., Hillaire, C., Daugas, J.-P., Arnold, M., Cachier, H., Evin, J., Fortin, P., Oberlin, C., Tisnerat, N., Valladas, H., 1995. Les peintures paléolithiques de la grotte Chauvet-Pont d'Arc, à Vallon-Pont d'Arc (Ardèche, France): datations directes et indirectes par la méthode du radiocarbone. C. R. Acad. Sci. 1133–1140 Paris IIA.
Conn, H.W., 1966. Barometric wind in Wind and Jewel Caves. South Dakota. Bull. Nat. Speleol. Soc. 28, 55–69.
Crockett, R.G.M., Perrier, F., Richon, P., 2010. Spectral-decomposition techniques for the identification of periodic and anomalous phenomena in radon time-series. Nat. Hazards Earth Syst. Sci. 10, 559–564.
Crockett, R., 2019. A primer on Fourier analysis for the Geosciences. Cambridge University Press, United Kingdom.
Crouzeix, C., Le Mouël, J.-L., Perrier, F., Richon, P., Morat, P., 2003. Long term thermal evolution and effect of low power heating in an underground quarry. C. R. Geosci. 335, 345–354.
Crouzeix, C., Le Mouël, J.-L., Perrier, F., Shnirman, M.G., Blanter, E., 2006. Long-term persistence of the spatial organization of temperature fluctuation lifetime in turbulent air avalanches. Phys. Rev. E 74, 036308.
Dal Moro, G., Zadro, M., 1998. Subsurface deformations induced by rainfall and atmospheric pressure: tilt/strain measurements in the NE-Italy seismic area. Earth Planet. Sci. Lett. 164, 193–203.

De Freitas, C.R., Littlejohn, R.N., 1987. Cave climate: assessment of heat and moisture exchange. J. Clim. 7, 553–569.
De Freitas, C.R., Littlejohn, R.N., Clarkson, T.S., Kristament, I.S., 1982. Cave climate: assessment of airflow and ventilation. J. Clim. 2, 383–397.
Denis, A., Lastennet, R., Humeau, F., Malaurent, P., 2005. Identification of functional relationships between atmospheric pressure and CO_2 in the cave of Lascaux using the concept of entropy of curves. Geophys. Res. Lett. 32, L05810.
Dominguez-Villar, D., Lojen, S., Krklec, K., Baker, A., Fairchild, I.J., 2015. Is global warming affecting cave temperatures? Experimental and model data from a paradigmatic case study. Clim. Dyn. 45, 569–581.
d'Oreye de Lantremange, N., Zuern, W., 2006. Quarter-diurnal tides observed with a long-base water-tube tiltmeter in the Grand Duchy of Luxembourg. J. Geodyn. 41, 175–182.
Drăgușin, V., Tîrlă, L., Cadicheanu, N., Ersek, V., Mirea, I.-C., 2018. Caves as observatories for atmosphere thermal tides: an example from Ascunsă Cave. Romania. Int. J. Speleol. 47, 113–117.
Dupray, F., Li, C., Laloui, L., 2013. THM coupling sensitivity analysis in geological nuclear waste storage. Eng. Geol. 163, 113–121.
Ferguson, G., Woodbury, A.D., 2004. Subsurface heat flow in an urban environment. J. Geophys. Res. 109, B02402.
Fernandez, P.L., Gutierrez, I., Quindos, L.S., Soto, J., Villar, E., 1986. Natural ventilation of the Paintings Room in the Altamira cave. Nature 321, 586–588.
Fernandez-Cortes, A., Cuezva, S., Sanchez-Moral, S., Cañaveras, J.C., Porca, E., Jurado, V., Martin-Sanchez, P.M., Saiz-Jimenez, C., 2011. Detection of human-induced environmental disturbances in a show cave. Environ. Sci. Pollut. Res. 18, 1037–1045.
Genty, D., 2008. Palaeoclimate research in Villars Cave (Dordogne, SW-France). Int. J. Speleol. 37, 173–191.
Genty, D., Baker, A., Vokal, B., 2001. Intra- and inter-annual growth rate of modern stalagmites. Chem. Geol. 176, 191–212.
Genty, D., Deflandre, G., 1998. Drip flow variations under a stalactite of the Père Noël cave (Belgium). Evidence of seasonal variations and air pressure constraints. J. Hydrol. 211, 208–232.
Ghil, M., Allen, M.R., Dettinger, M.D., Ide, K., Kondrashov, D., Mann, M.E., Roberson, A.W., Saunders, A., Tian, Y., Varadi, F., Yiou, P., 2002. Advanced spectral methods for climatic time series. Rev. Geophys. 40, 1003.
Guineau, B., Lorblanchet, M., Gratuze, B., Dulin, L., Roger, P., Akrich, R., Muller, F., 2001. Manganese black pigments in prehistoric paintings: The case of the black frieze of Pech Merle (France). Archaeometry 43, 211–225.
Hoffmann, D.L., Standish, C.D., García-Diez, M., Pettitt, P.B., Milton, J.A., Zilhão, J., Alcolea-González, J.J., Cantalejo-Duarte, P., Collao, H., de Balbín, R., Lorblanchet, M., Ramos-Muñoz, J., Weniger, G.-Ch., Pike, A.W.G., 2018. U-Th dating of carbonate crusts reveals Neanderthal origin of Iberian cave art. Science 359, 912–915.
Houillon, N., Lastennet, R., Denis, A., Malaurent, P., Minvielle, S., Peyraube, N., 2017. Assessing cave internal aerology in understanding carbon dioxide (CO_2) dynamics: Implications on calcite mass variation on the wall of Lascaux Cave (France). Environ. Earth Sci. 76, 170.
Irvine, D.J., Kurylyk, B.L., Cartwright, I., Bonham, M., Post, V.E.A., Banks, E.W., Simmons, C.T., 2017. Groundwater flow estimation using temperature-depth profiles in a complex environment and a changing climate. Sci. Total Environ. 574, 272–281.
Jaubert, J., Verheyden, S., Genty, D., Soulier, M., Cheng, H., Blamart, D., Burlet, C., Camus, H., Delaby, S., Deldicque, D., Lawrence Edwards, R., Ferrier, C., Lacrampe-Cuyaubère, F., Lévêque, F., Maksud, F., Mora, P., Muth, X., Régnier, É., Rouzaud, J.-N., Santos, F., 2016. Early Neanderthal constructions deep in Bruniquel Cave in southwestern France. Nature 534, 111–115.
Kukuljan, L., Gabrovšek, F., Covingon, M.D., Johnston, V.E., 2021. CO_2 dynamics and heterogeneity in a cave atmosphere: role of ventilation patterns and airflow pathways. Theor. Appl. Climatol. 146, 91–109.
Lin, H., 2010. Earth's Critical Zone and hydropedology: concepts, characteristics, and advances. Hydrol. Earth Syst. Sci. 14, 25–45.
Lindzen, R.S., Chapman, S., 1969. Atmospheric tides. Space Sci. Rev. 10, 3–188.
Lorblanchet, M., 2010. Art pariétal: Grottes ornées du Quercy. Editions du Rouergue, Rodez. In French.
Lovill, S.M., Hahm, W.J., Dietrich, W.E., 2018. Drainage from the critical zone: Lithologic controls on the persistence and spatial extent of wetted channels during the summer dry season. Water Resour. Res. 54, 5702–5726.
Luetscher, M., Lismonde, B., Jeannin, P.-Y., 2008. Heat exchanges in the heterothermic zone of a karst system: Monlesi case, Swiss Jura Mountains. J. Geophys. Res. 113, F02025.
Mangin, A., D'Hulst, D., 1996. Fréquentation des grottes touristiques et conservation, Méthode d'approche pour en étudier les effets et proposer une règlementation. International Symposium Show Caves and Environmental Monitoring, Cueno, Italy, 1995. A.A. Cigna (Ed.), 137–167.
Mangin, A., Bourges, F., d'Hulst, D., 1999. Painted caves conservation: A stability problem in a natural system (the example of the prehistoric cave of Gargas, French Pyrenees). C. R. Acad. Sci. Paris 328, 295–301.
Mejía-Ortiz, L., Christman, M.C., Pipan, T., Culver, D.C., 2020. What's the temperature in tropical caves? Plos One 15, e0237051.
Niebauer, T.M., MacQueen, J., Aliod, D., Francis, O., 2011. Monitoring earthquakes with gravity meters. Geodes. Geodyn. 2, 71–75.
Novitsky, C.G., Holbrook, W.S., Carr, B.J., Pasquet, S., Okaya, D., Flinchum, B.A., 2018. Mapping inherited fractures in the critical zone using seismic anisotropy from circular surveys. Geophys. Res. Lett. 45, 3126–3135.
Pastoors, A., Lenssen-Erz, T., Breuckmann, B., Ciqae, T., Kxunta, U., Rieke-Zapp, D., Thao, T., 2017. Experience-based reading of Pleistocene human footprints in Pech-Merle. Quat. Int. 430, 155–162.
Perrier, F., Bourges, F., Girault, F., Le Mouël J.-L., Genty, D., Lartiges B., Losno, R., Bonnet, S. Temperature variations in caves induced by atmospheric pressure variations, 2: Unveiling hidden thermal signals. Geosys. Geoenviron. This issue.
Perrier, F., Le Mouël, J.-L., 2016. Stationary and transient thermal states of barometric pumping in the access pit of an underground quarry. Sci. Total Environ. 550, 1044–1056.
Perrier, F., Le Mouël, J.-L., Kossobokov, V., Crouzeix, C., Morat, P., Richon, P., 2005b. Properties of turbulent air avalanches in a vertical pit. Eur. Phys. J. B 46, 563–579.
Perrier, F., Le Mouël, J.-L., Poirier, J.-P., Shnirman, M.G., 2005a. Long-term climate change and surface versus underground temperature measurements in Paris. Int. J. Clim. 25, 1619–1631.
Perrier, F., Le Mouël, J.-L., Richon, P., 2010. Spatial and temporal dependence of temperature variations induced by atmospheric pressure variations in shallow underground cavities. Pure Appl. Geophys. 167, 253–276.
Perrier, F., Morat, P., Le Mouël, J.-L., 2001. Pressure induced temperature variations in an underground quarry. Earth Planet. Sci. Lett. 191, 145–156.
Perrier, F., Morat, P., Le Mouël, J.-L., 2002. Dynamics of air avalanches in the access pit of an underground quarry. Phys. Rev. Lett. 89, 134501.
Perrier, F., Morat, P., Yoshino, T., Sano, O., Utada, H., Gensane, O., Le Mouël, J.-L., 2004a. Seasonal thermal signatures of heat transfer by water exchange in an underground vault. Geophys. J. Int. 158, 372–384.
Perrier, F., Richon, P., 2010. Spatiotemporal variation of radon and carbon dioxide concentrations in an underground quarry: Coupled processes of natural ventilation, barometric pumping and internal mixing. J. Environ. Radioact. 101, 279–296.
Perrier, F., Richon, P., Crouzeix, C., Morat, P., Le Mouël, J.-L., 2004b. Radon-222 signatures of natural ventilation regimes in an underground quarry. J. Environ. Radioact. 71, 17–32.
Perrier, F., Richon, P., Gautam, U., Tiwari, D.R., Shrestha, P., Sapkota, S.N., 2007. Seasonal variations of natural ventilation and radon-222 exhalation flux in a slightly rising dead-end tunnel. J. Environ. Radioact. 97, 220–235.
Perrier, F., Richon, P., Sabroux, J.-C., 2005c. Modelling the effect of air exchange on radon-222 and its progeny concentration in a tunnel atmosphere. Sci. Total Environ. 350, 136–150.
Quilty, E.G., Roeloffs, E., 1991. Removal of barometric pressure response from water level data. J. Geophys. Res. 96 (10), 209–210 218.
Quindos, L.S., Bonet, A., Diaz-Caneja, N., Fernandez, P.L., Gutierrez, I., Solana, J.R., Soto, J., Villar, E., 1987. Study of the environmental variables affecting the natural preservation of the Altamira Cave paintings located at Santillana Del Mar. Spain. Atmospheric Environ. 21, 551–560.
Rasmussen, C., Troch, P.A., Chorover, J., Brooks, P., Pelletier, J., Huxman, T.E., 2011. An open system framework for integrating critical zone structure and function. Biogeochemistry 102, 15–29.
Rau, G.C., Cuthberg, M.O., Andersen, M.S., Baker, A., Rutlidge, H., Markowska, M., Roshan, H., Marjo, C.E., Graham, P.W., Acworth, R.I., 2015. Controls on cave drip water temperature and implications for speleothem-based paleoclimate reconstructions. Quat. Sci. Rev. 127, 19–36.
Ravbar, N., Kosutnik, J., 2014. Variations of karst underground air temperature induced by various factors (Cave of Županova jama. Central Slovenia). Theor. Appl. Climatol. 116, 327–341.
Richon, P., Perrier, F., Pili, E., Sabroux, J.-C., 2009. Detectability and significance of 12 hr barometric tide in radon-222 signal, dripwater flow rate, air temperature and carbon dioxide concentration in an underground tunnel. Geophys. J. Int. 176, 683–694.
Sáez, M., Mangiarotti, S., Cuezva, S., Fernández-Cortés, A., Molero, B., Sánchez–Moral, S., Benavente, D., 2021. Global models for ^{222}Rn and CO_2 concentrations in the Cave of Altamira. Theor. Appl. Clim. 143, 603–626.
Schill, E., Meixner, J., Meller, C., Grimm, M., Grimmer, J.C., Stober, I., Kohl, T., 2016. Criteria and geological setting for the generic geothermal underground research laboratory. GEOLAB. Geotherm. Energy 4, 7.
Šebela, S., Turk, J., 2011. Local characteristics of Postojna Cave climate, air temperature, and pressure monitoring. Theor. Appl. Climatol. 105, 371–386.
Sims, W.E., Bostick Jr., F.X., Smith, H.W., 1971. The estimation of magnetotelluric impedance tensor elements from measured data. Geophysics 36, 938–942.
Smithson, P.A., 1991. Inter-relationships between cave and outside air temperatures. Theor. Appl. Climatol. 44, 65–73.
Sondag, F., van Ruymbeke, M., Soubiès, F., Santos, R., Somerhausen, A., Seidel, A., Boggiani, P., 2003. Monitoring present day climatic conditions in tropical caves using an Environmental Data Acquisition System (EDAS). J. Hydrol. 273, 103–118.
Trique, M., Richon, P., Perrier, F., Avouac, J.-P., Sabroux, J.-C., 1999. Radon emanation and electric potential variations associated with transient deformation near reservoir lakes. Nature 399, 137–141.
Turcotte, D.L., 1992. Fractals and chaos in geology and geophysics. Cambridge University Press, New York.
Villar, E., Bonet, A., Diaz-Caneja, B., Fernandez, P.L., Gutierrez, I., Quindos, L.S., Solana, J.R., Soto, J., 1984. Ambient temperature variations in the hall of paintings of Altamira cave due to the presence of visitors. Cave Sci. 11, 99–104.
Wigley, T.M.L., 1967. Non-steady flow through a porous medium and cave breathing. J. Geophys. Res. 72, 3199–3205.
Wigley, T.M.L., Brown, M.C., 1971. Geophysical applications of heat and mass transfer in turbulent pipe flow. Boundary Layer Meteorol. 1, 300–320.
Xu, X., Liu, W., 2017. The global distribution of Earth's critical zone and its controlling factors. Geophys. Res. Lett. 44, 3201–3208.
Zhang, Z., Chen, X., Soulsby, C., 2017. Catchment-scale conceptual modelling of water and solute transport in the dual flow system of the karst critical zone. Hydrol. Process. 31, 3421–3436.